On the impact of operating condition and testing environment on the noise sources in an industrial engine cooling fan

Terms of use:

Publisher copyright

(Article begins on next page)

23 November 2024

On the impact of operating condition and testing environment on the noise sources in an industrial engine cooling fan

Francesco Bellelli *, Renzo Arina, Francesco Avallone

Department of Mechanical and Aerospace Engineering, Politecnico di Torino, Corso Duca degli Abruzzi 24, 10129, Torino, Italy

ARTICLE INFO

ABSTRACT

Engine cooling fan noise is a relevant issue for manufacturers. It is well known that both the operating point and testing environment can affect the noise generation mechanisms and, consequently, the measured noise may change. Therefore, these aspects are investigated on a reference industrial fan, for which experimental data exists, using high-fidelity numerical simulations based on the lattice-Boltzmann method. Two operating conditions, namely the free blowing and the maximum efficiency ones, and three testing environments are analyzed: (i) a conventional semi-anechoic room, (ii) an ideal free field environment, and (iii) a testing environment resembling an anechoic aeraulic facility. For cases (i) and (ii) no pressure difference across the fan is imposed, while, for case (iii), a pressure difference across the fan can be imposed. For the latter, the impact of a fully reflective and fully absorbing wall separating the two regions upstream and downstream of the fan is analyzed. At free blowing conditions, the flow over the blades is largely separated. When the blade passes through a blockage region, because of the presence of a honeycomb-like structure needed for structural purposes, it experiences a prominent loading hump. The far-field noise, at a listener located along the axis of rotation, is therefore highly tonal, with a clear peak at the blade passing frequency tone. When the same fan is tested in a free field environment, it is found that there is a difference in the acoustic pressure at higher harmonics of the blade passing frequency due to the presence of flow recirculations in the anechoic room. Placing a thin wall across the fan increases the mass flow rate, for a given rotational speed, which results in a more severe flow separation over the blades and, therefore a higher tone prominence at the blade passing frequency. If the thin wall is modeled as a sound-absorbing wall, there is a drop of the overall sound pressure level of about 2 dBA. When the fan is tested at its maximum efficiency, i.e., nonzero pressure difference across the fan, it is found that the blockage effect is less relevant. The main noise generation mechanism is the back-flow vortex induced by the pressure difference across the fan interacting with the blade tip leading edge.

1. Introduction

Automotive thermal engines and electric motors need a cooling fan package. Its first design purpose has always been aerodynamic efficiency, but since electric motors are replacing thermal engines there is an increasing need to reduce noise emissions. Therefore, research on noise generation mechanisms [1,2] and reduction techniques [3,4] has rapidly gained importance. Researchers have put their effort into assessing the main noise generation mechanisms and identifying noise reduction solutions that can be both affordable and efficient.

Engine cooling fans are characterized by many noise sources; some of them can be classified as airfoil self-noise, loading, and thickness noise and depend on the operating conditions and geometry of the isolated blades [5], while others depend on their installation within the cooling module and the presence of stator vanes.

Thickness noise, due to air displacement induced by blade passage, is usually negligible at low Mach numbers but it can be relevant for fans with high solidity [6]. Loading noise instead depends on the forces exerted by the blade. When the blade loading is constant during the rotation, the noise source is named as steady loading noise, and the resulting noise spectrum is characterized by a tonal peak at the blade passing frequency (BPF) equal to $N_b\Omega/60$ and its harmonics, following a dipolar directivity pattern. The amplitude of the tonal peak decreases with increasing BPF harmonics. If, on the other hand, the inflow is not uniform or turbulent, then the blade loading varies during a rotation causing unsteady loading or impingement noise respectively. This usually re-

---

* Corresponding author.

E-mail address: francesco.bellelli@polito.it (F. Bellelli).

Nomenclature

BPF	Blade Passing Frequency	
LBM	Lattice-Boltzmann Method	
VR	Variable Resolution	
PSD	Power Spectral Density	
FWH	Ffwocs-Williams and Hakwings	
$\bar{q}$	Mean of q	
$\tilde{q}$	Fourier Transform of q	
q_σ	Standard deviation of q	
i	Imaginary unit	
vox	Number of voxels in the finest VR region	
x, y, z	Axial, horizontal, and vertical coordinates	$[m]$
$r = \sqrt{y^2 + z^2}$	Radial position in the x plane	$[m]$
D	Fan diameter	$[m]$
c	Blade chord	$[m]$
Ω	Fan angular velocity	$[RPM]$
N_b	Number of rotor blades	$[-]$
N_v	Number of stator vanes	$[-]$
f	Frequency	$[Hz]$
p	Static pressure	$[Pa]$
$SPL = 20 \log_{10}\left(\frac{p_{rms}}{2 \cdot 10^{-5}}\right)$	Sound Pressure Level	$[dBA]$

$OSPL = 10 \log_{10}\left(\sum_i 10^{\frac{SPL(f_i)}{10}}\right)$	Overall Sound Pressure Level	$[dBA]$
Δp	Pressure difference across the fan	$[Pa]$
$\dot{m}$	Mass flow rate across the fan	$[kg/s]$
Q	Aerodynamic torque	$[Nm]$
$v_{tip} = \Omega \frac{D}{2}$	Tip velocity	$[m/s]$
u, v, w	Axial, horizontal, and vertical velocities	$[m/s]$
$p_{tip}^\circ = \frac{1}{2}\rho v_{tip}^2$	Tip dynamic pressure	$[Pa]$
$\psi = \frac{2\Delta p}{\rho v_{tip}^2}$	Load coefficient	$[-]$
$\varphi = \frac{4\dot{V}}{\pi(D^2 - D_{hub}^2)v_{tip}}$	Flow coefficient	$[-]$
$c_p = \frac{2(p - p_{amb})}{\rho_{amb} v_{tip}^2}$	Pressure coefficient	$[-]$
a	Acoustic absorption coefficient	$[-]$
k	Turbulent kinetic energy	$[m^2/s^2]$
ϵ	Turbulence dissipation rate	$[m^2/s^3]$
$Tu = \sqrt{\frac{2k}{3(\bar{u}^2 + \bar{v}^2 + \bar{w}^2)}}$	Turbulence intensity	$[\%]$
$\Lambda = \frac{0.085 k^{1.5}}{\epsilon}$	Turbulent integral length scale	$[m]$

sults in an increase of noise intensity at the BPF higher harmonics or a broadband hump [7]. While steady loading noise is conventionally mitigated by the uneven spacing of the blades [8] or by designing low-noise blades, the reduction of unsteady loading or impingement noise is more difficult because of the involved flow physics. For example, Magne et al. [9] found that the interaction of the back-flow, due to the pressure difference across the fan, with the blades is a major source of unsteady loading noise. Given the nature of this noise source, its reduction is technologically challenging. On the other hand, in the case of impingement noise due to turbulent inflow conditions, several solutions have been proposed. For example, Sun et al. [10] designed an ad hoc short inlet duct; Ocker et al. [11] applied porous materials at the leading edge of the blades; Chaitanya et al. [12], Ocker et al. [13] and Zhou et al. [4] designed wavy, slitted or bio-inspired leading edges. The latter solution can cause noise to increase at high frequencies.

Since the vast majority of cooling fans are equipped with stator vanes, noise from their interaction with rotor blades is generated [1]. The interaction is usually classified as "potential" and viscous. The former is due to the change in blade loading during the rotation because of the proximity of the stator vane. The latter, on the other hand, arises from the impingement of the blade wakes on the stator vanes. A way to reduce interaction noise is to unevenly spacing both rotor blades and stator vanes. However, the benefits of such design are visible only at the operating design conditions [14]. It was also found that if stator vanes with different geometries are distributed along the azimuth, then additional discrete tones can appear [15,16] at frequencies different than the ones predicted using the Tyler and Sofrin rule for rotor-stator interaction [17].

A last but very relevant noise source is tip-clearance noise, generated by the coherent vortex structures that arise in the tip-gap region [18]. Its contribution to the far-field acoustics can be found in the sub-harmonic humps present in the spectrum [19]. It is usually mitigated by applying forward sweep to the blade geometry [20] or by introducing a rotating [21], or a stationary [22] ring on the rotor. Alternative approaches, that have been shown to be promising, are based on the installation of a bell-mouth inlet [23,24] or on adopting casing treatments [25].

It is important to mention that the integration of the various components of a cooling module might generate additional interactions that contribute to the far-field noise [26]. This aspect goes beyond the scope of the current paper and will not be further discussed.

The large variety of noise generation mechanisms present in cooling fans makes their acoustic optimization challenging. Furthermore, the relevance of one noise source with respect to the others varies depending on the operating condition. Therefore, their characterization using experiments or numerical simulations is essential.

Several experimental environments can be used to measure the far-field noise generated by such systems in order to test them at different operating conditions [27]. A way to measure the far-field noise is to perform measurements in an anechoic room where a pressure difference across the fan can be imposed, as done in anechoic aeraulic facilities. In this case, the fan or the entire cooling package is placed across a wall, ideally equipped with sound-absorbing material, and placed in an anechoic environment; the flow field near the walls, either absorbing or not, can affect, through secondary vortices, the unsteady loading and therefore the far-field noise [28,29]. It has been shown by Lu et al. [30] that this testing environment is the one that provides data that are the closest to the one measured when the cooling module is installed within the vehicle. However, in some cases, measurements are carried out in an anechoic room where no pressure difference can be imposed and the fan is tested at free blowing condition. In this case, the fan is operated at off-design condition, therefore affecting the relevant noise generation mechanisms [27]. Additional effects, such as the flow recirculation within the anechoic room can further affect the far-field noise. As a matter of fact, Foss et al. [31] and Sturm et al. [32] showed that recirculation has a noticeable impact on the sound emission, despite the flow field and the loading history might show minor changes. These aspects, which have not been widely addressed in the scientific literature, can have a large impact on the measured noise and far-field directivity [28,29].

This paper aims to characterize the far-field noise of a reference industrial engine cooling fan, for which experimental data were made available, by assessing how the noise generation mechanisms vary with the operating condition and testing environment. These include variations in the testing environment from a semi-anechoic chamber to a free field ambient, and changing the operating point from free blowing to maximum efficiency. For this purpose, scale-resolved high-fidelity numerical simulations are carried out with the lattice-Boltzmann method (LBM). The results and findings presented in this paper are an extension of a conference paper presented by the authors at the 30th CEAS/AIAA Aeroacoustics Conference [33].

The rest of the paper is structured as follows: section 2 describes the methodology used to calculate hydrodynamic and acoustic fields numerically, section 3 briefly summarizes the experimental setup used to validate the numerical calculations, which are presented in detail in section 4. The grid convergence study and the validation of the numerical simulations against the experiments is discussed in section 5. Section 6 discusses the obtained results, while the main conclusions and future work are reported in section 7.

2. Methodology

The flow field is computed using the commercial software 3DS PowerFLOW version 6, based on the LBM [34]. The solver has been widely used to study the aerodynamics and aeroacoustics of low-speed fans for automotive applications [20,35–37].

The continuous Boltzmann equation is:

$$\frac{\partial f}{\partial t} + c\frac{\partial f}{\partial x} + \frac{F}{m_f}\frac{\partial f}{\partial c} = \mathcal{C}. \tag{1}$$

In the equation, $f(\vec{x}, \vec{c}, t)$ is the particle distribution function, which represents the probability that at time t there is a particle at position $\vec{x}$ with microscopic velocity $\vec{c}$. F is the external force, m_f is the molecular weight of the fluid, and $\mathcal{C}$ is the so-called collision operator, which accounts for the distribution function variation due to elastic collisions between two particles. Since the collisions are elastic, mass, momentum, and kinetic energy must be conserved. The Bhatnagar, Gross, Krook (BKG) collision operator [38] is adopted

$$\mathcal{C} = -\frac{1}{\tau}(f - f^{eq}), \tag{2}$$

where τ is the relaxation time and f^{eq} is the Maxwell-Boltzmann equilibrium distribution function, to which f tends. It has been shown that, by performing a Chapman-Enskog expansion [39], it is possible to recover the Navier-Stokes equations from Eq. (1) for low Mach numbers.

The Boltzmann equation is numerically discretized in space by dividing the computational domain into cubic lattices, called voxels. In every voxel, particles are set to move only in a fixed number of directions. In its low Mach number solver version, adopted in this work, PowerFLOW implements a model with 19 discrete velocity directions in three dimensions [40]. The discretized Boltzmann equation is written for every voxel and solved through two subsequent steps: collision and streaming on the near neighbors. To consider the possibility of simulating rotating parts, a sliding mesh approach is used [41].

To directly resolve only the turbulence scales beyond a certain threshold, a very large eddy simulation (VLES) approach is used. This can be done by adjusting the relaxation time; the effective relaxation time can be written as:

$$\tau_{eff} = \tau + \tau_{turb}. \tag{3}$$

The subgrid model is derived from the renormalization group $k - \epsilon$ transport equations (RNG $k - \epsilon$) [42]. To further reduce the computational cost, the flow field in the vicinity of solid walls is approximated through the pressure-gradient extended wall model (PGE-WM) [43], an extension of the generalized wall model proposed by Launder and Spalding [44].

The advantages of LBM rely upon the fact that it is not necessary to generate complex and unstructured grids since the computational domain is simply divided into cubic lattices, and that it is a highly parallelizable method, due to the explicit time-marching method used to solve numerically Eq. (1).

The LBM is particularly suited for aeroacoustic applications since it is intrinsically compressible and therefore allows for direct aeroacoustic computation. This is possible thanks to the lower numerical diffusion and dispersion against the most common CFD schemes based on the Navier-Stokes equations. Indeed, 15 voxels per wavelength are sufficient to compute the acoustic signature from the unsteady flow field directly.

The far-field acoustics is directly computed from the pressure fluctuations recorded at specific locations as will be discussed in section 4. To discriminate the contribution of each solid surface on the far-field noise, the Ffwocs-Williams and Hakwings (FWH) acoustic analogy [45] is applied with a forward-time solution [46] based on formulation 1A by Farassat [47].

In addition to the data provided directly by the simulations, the mean and instantaneous contribution at a given virtual microphone of every surface of which the engine cooling fan is composed has been computed through the *OptydB-pfnoisescan* [48] tool. The resulting surface field is shown in frequency bands centered at the BPF and its first harmonic as dB/m^2 and allows further localization of the regions of the solid surface that mainly contribute to the far-field noise. Such quantity can be interpreted as the noise contribution of each surface element at the considered virtual probe. This paper reports only the mean values, while for the instantaneous ones, the reader is referred to the videos attached to the web version.

3. Engine cooling fan geometry and tested operating conditions

The engine cooling module consists of a fan with $N_b = 11$ unevenly spaced blades connected to a ring, a hub, a driving electrical motor, $N_v = 20$ unevenly spaced stator vanes, and a shroud, as shown in Fig. 1a with different colors. The fan diameter is equal to 465 mm and the tip clearance is equal to 6.46% of the blade tip chord $c = 65$ mm, as shown in Fig. 1b. Since the fan is an industrial product, it is characterized using non-dimensional parameters.

Reference experimental data were acquired to validate the numerical simulations. Mass flow rate and torque were measured in an aeraulic facility, while acoustic measurements were performed in a semi-anechoic room. Both data were provided by the manufacturer.

Mass flow rate and torque measurements were carried out at two operating conditions: free blowing and maximum efficiency, corresponding to load coefficient $\psi = \frac{\Delta p}{\frac{1}{2}\rho v_{tip}^2}$ equal to 0 and 0.14 respectively.

The aeraulic facility is built according to the AMCA 210-99 standard. The pressure difference is set by depressurizing the upstream chamber and recorded by means of a pressure sensor. The volume flow rate is measured with a standardized volumetric flow meter, while the torque is measured with a torquemeter. The performances are recorded for a $3\,s$ interval, in which is ensured that the pressure difference relies in a 1% band of the desired value. During the performance test, the driving electric motor is supplied with constant shaft power, which results in different angular velocity values for the two investigated operating points.

Acoustic measurements were carried out only for the free blowing condition because they were measured in a semi-anechoic room without any wind tunnel. The dimensions of the semi-anechoic room are $5 \times 5 \times 3\,$m^3 and the floor is at a distance of $z/D = 3.23$ from the fan center. The semi-anechoic room is equipped with two 1/2" PCB Piezotronics far-field microphones placed upstream to the fan, which is situated in the center of the chamber. One of the two microphones is placed along the fan axis and the other one at 90° with respect to the first. The pressure signal has been acquired for $20\,s$ at a sampling frequency of $25.6\,kHz$ and its spectral content computed through the Welch averaging algorithm [49] with 1280 Hamming windows (each window covers 2.5 fan revolutions) and 50% of overlap, resulting in a frequency resolution of $11.8\,Hz$. These parameters have been chosen to ensure that the experimental and the corresponding numerical signals have the same characteristics so that a fair comparison can be made between them.

A summary of the settings for each operating condition and the available experimental data is reported in Table 1.
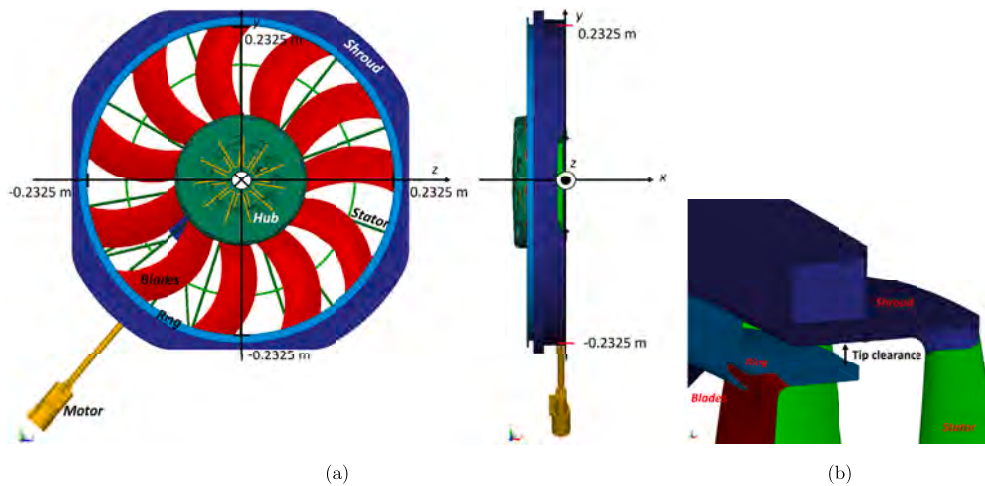
Fig. 1. Tested automotive engine cooling module. The main parts in which the fan consists are shown with different colors. (a): Cooling module. (b): Tip clearance detail.

Table 1
Operating condition settings and available experimental data. A checkmark indicates that the experiment has been performed, while a cross indicates that it has not been performed.

	Free blowing	Max efficiency
ψ	0	0.14
φ	0.19	0.10
Ω [RPM]	3048	2868
Performance Measurements	✓	✓
Acoustic Measurements	✓	✗

4. Numerical setup

The cooling fan without the heat exchanger is analyzed. The geometry adopted is the same measured experimentally (Fig. 1a) and the CAD has been provided by the manufacturer.

Four computational domains are investigated: (i) a semi-anechoic room configuration; (ii) a free field configuration; (iii) a configuration that allows to impose a delta pressure across the fan, as in an ideal aeraulic facility, to study the maximum efficiency configuration neglecting flow recirculation as in a conventional room. For the latter, the wall separating the two environments is modeled both as fully reflective ($a = 0$) and fully absorbing ($a = 1$).

The computational domain used to simulate the semi-anechoic room environment is depicted in Fig. 2. A large fluid domain of $63 \times 63 \times 63$ m^3 is built containing the semi-anechoic room. The semi-anechoic room walls, of the same size as the experimental one, are modeled as an equivalent porous medium with viscous resistance equal to 50000 1/s. The floor of the domain is modeled as a solid reflective wall to mimic the experimental facility. Outside the semi-anechoic room, several variable resolution (VR) regions are placed. Between one VR region and the adjacent one the voxel size changes by a factor of 2. Furthermore, outside the semi-anechoic room a sponge region is defined by an artificial change of viscosity of a factor of 100 with an exponential function going from the inner to the outer region shown in Fig. 2. Both the increase in voxel size and the sponge region are used to mitigate reflections of acoustics waves at the boundaries of the domain. At both inlet and outlet boundaries, static ambient pressure boundary condition is applied. The ceiling of the simulation domain is modeled as a solid fully reflecting wall.

Within the semi-anechoic room region, a discretization strategy based on 11 VRs is adopted as shown in Fig. 3. The regions with maximum resolutions are set around the rotating blades and near the tip gap region, where for the most refined case there are 11 voxels in the
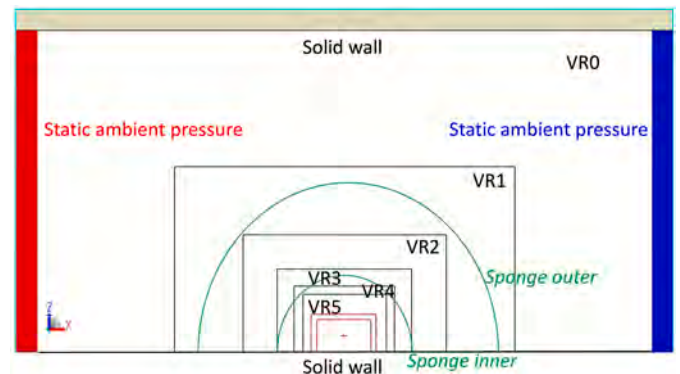

Fig. 2. Computational domain at free blowing conditions in the semi-anechoic room with outer VR regions. The inner VR regions are not shown due to their smaller dimensions with respect to the simulation volume size shown in the figure.

tip clearance. The resolution in the tip gap region is similar to the one adopted by Avallone et al. [50].

The other two testing configurations, i.e., free field and the case with the wall, are obtained by doubling the computational domain in the z direction as shown in Fig. 4a and Fig. 4b, respectively. The thin wall across the fan is modeled as fully reflective ($a = 0$) or as fully absorbing ($a = 1$); this allows studying the case when the fan is tested in a very large acoustically untreated aeraulic facility or in an anechoic one. For both cases, the porous and solid walls used in the semi-anechoic room environment are removed, while the sponge region starting at VR5 is kept the same. The boundary conditions are kept the same as for the semi-anechoic configuration for the free blowing case, while a mass-flow boundary condition is imposed upstream to simulate the maximum efficiency operating condition. For both cases, the discretization strategy within VR5 is the same as the one described for the semi-anechoic testing environment.

A physical time of at least 20 revolutions is simulated for every condition; data are acquired during the last 10 revolutions. Three simulations have been performed at three different resolutions equal to $600\,vox/D$, $1000\,vox/D$, and $1200\,vox/D$ in the finest VR region. The free blowing condition is used for the grid convergence study because of the availability of both aerodynamic and acoustic experimental data as it will be shown in section 5.

Pressure and velocity are sampled on two perpendicular planes located respectively at $y/D = 0$ and $z/D = 0$ at $48,000\,Hz$. Three planes parallel to the fan disk, located at $x/D = -0.12$, $x/D = -0.06$, and
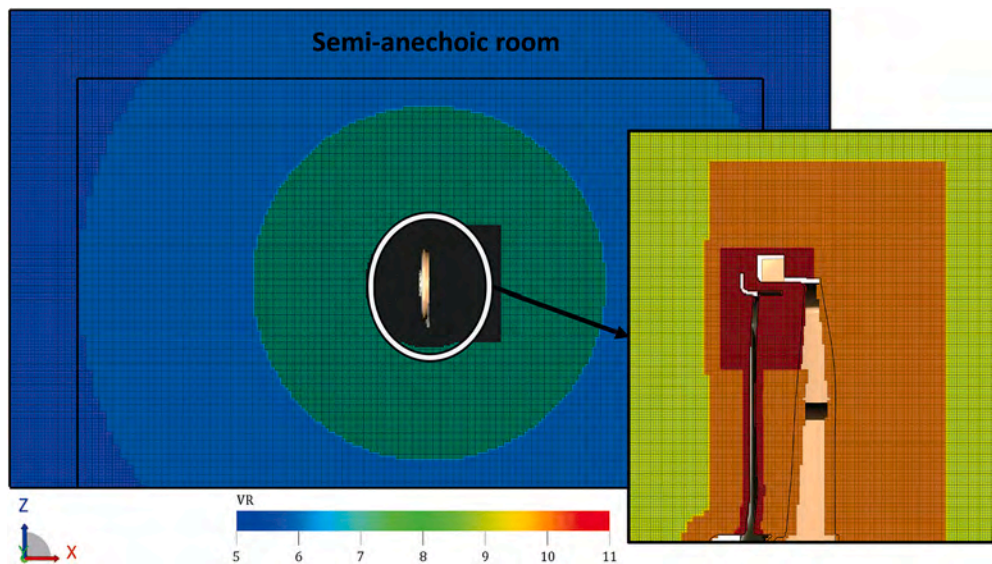
Fig. 3. Detail of the 11 VR regions in the computational domain at free blowing conditions in the semi-anechoic room. Computational grids for the other simulated cases are not shown because they are the same.
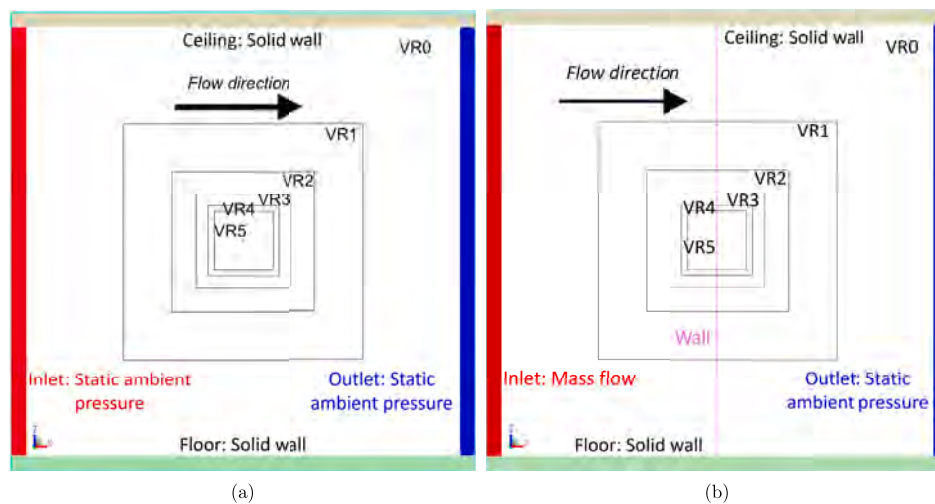

Fig. 4. (a): Sketch of the free field domain used for the free blowing case to compare against the semi-anechoic environment (Semi-anechoic and Free field cases in the following text). (b): Sketch of the free field domain used to assess the effects of the thin wall and of the operating condition (Free field - Wall, Free blowing, and Max efficiency cases in the following text).

$x/D = 0$, are sampled with a frequency equal to $3,000\,Hz$, to compute phase-locked flow fields. The three locations correspond to just upstream the sliding mesh region, the interstage between rotor and stator, and downstream the stator vanes trailing edge. Moreover, a small volume around the fan module is sampled at a frequency of $755\,Hz$. All the solid surfaces of the cooling module are sampled at a frequency of $48,000\,Hz$ and are used as input to the FWH acoustic analogy with the solid formulation.

Integral quantities such as blade loading, torque, and mass flow rate are also sampled. The mass flow is sampled with a frequency of $48,000\,Hz$ using the three planes located at $x/D = -0.17$, $x/D = -0.06$, and $x = 0/D$. The upstream plane is at a different location with respect to the one used to compute phase-locked because the plane at $x/D = -0.12$ intersects the solid region of the hub; therefore, it has been chosen to sample the mass flow rate on a surface slightly upstream.

Finally, a fully circular array of 12 equally spaced far-field probes located in the plane $z/D = 0$ at a radius $r/D = 2.15$ far from the fan center is used to sample directly the acoustic field from the simulations. Two of the probes are placed at the same locations as in the experiments in order to perform a validation of the numerical simulations. The spectral content of these signals is computed through the Welch averaging algorithm [49] with 8 Hamming windows and 50% of overlap, resulting in a frequency resolution of $11.8\,Hz$, so that a fair comparison can be made with the experimental signals, as explained in the previous section.

5. Grid convergence and numerical setup validation

First, it is established the resolution for which grid independence is achieved; this is done for the semi-anechoic domain at free blowing conditions because of the availability of experimental data. The ratio of mass flow rate through the fan section and torque obtained from the numerical simulations with the experimental ones are shown in Fig. 5 for the three resolutions. The "Inf" values are obtained through Richardson extrapolation [51] with a refinement ratio $r = 2$ and order of convergence $p = 3$ as done in previous studies with the same solver [52]. The figure shows that grid convergence is reached for the finest resolution case, as the extrapolated values are sufficiently close to the finest resolution. The grid convergence index (GCI) for both quantities is sufficiently small and the ratio R computed as
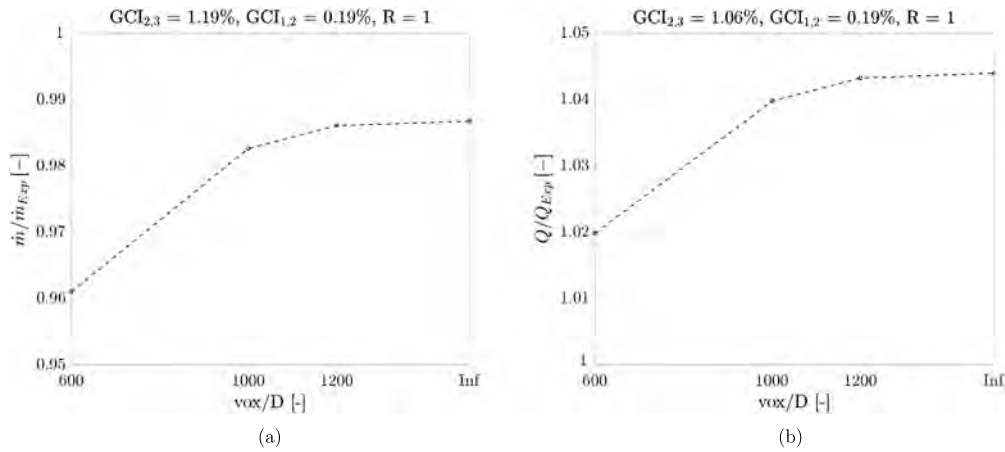
Fig. 5. Grid independence study for the semi-anechoic chamber configuration and free blowing condition. (a): The ratio of the mass flow rate computed from the numerical simulations with the experimental one. (b): The ratio of the torque computed from the numerical simulations with respect to the experimental one. "Inf" values are obtained through a Richardson extrapolation [51].
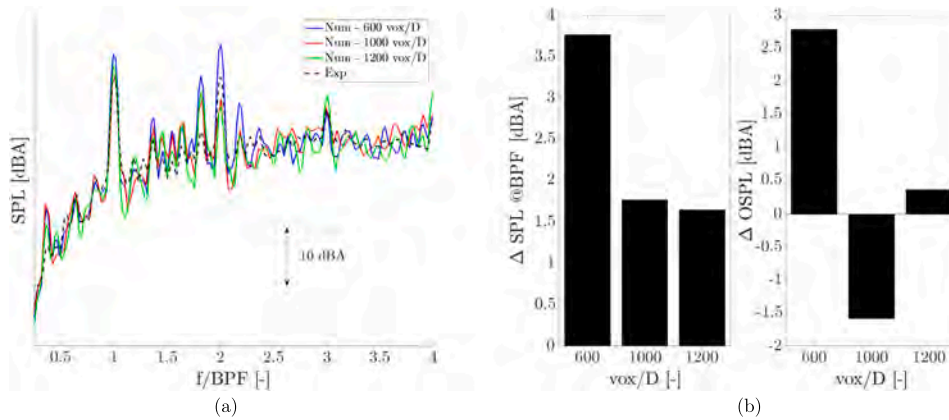

Fig. 6. Grid independence study and comparison with the experimental data of the far-field acoustics for the semi-anechoic chamber configuration and free blowing conditions. (a): Sound Pressure Level in dBA obtained at $2.15D$ by averaging the results from all the measurement points upstream of the fan. (b): Difference between the numerical and experimental results of the SPL in dBA at the first BPF and in terms of OSPL. The OSPL is computed in the frequency range between $f/BPF = 0.25$ and $f/BPF = 4$.

$$R = \frac{GCI_{2,3}}{r^p GCI_{1,2}} \tag{4}$$

is sufficiently close to $R = 1$, in accordance to what stated by Roache [53].

The mass flow rate differs of 1% with respect to the experimental one, while the torque is about 5% higher than the experimental one, similar to what found in other works in the literature [54].

After having established convergence for the integral quantities, the same is done for the far-field noise. The far-field noise spectra obtained $2.15D$ upstream of the fan from the direct probe, at the three resolutions, are compared against the experimental one in Fig. 6a by averaging the results from the front and lateral probes. The differences between the experiments and the simulations at the first BPF and in terms of OSPL differences are shown in Fig. 6b. The OSPL is computed in the range $0.25 < f/BPF < 4$.

A good agreement between experiments and numerical calculations is evident in Fig. 6a; the BPF tone can be correctly predicted within 1.5 dBA (as reported in Fig. 6b), while the second harmonic ($f/BPF = 2$) is under predicted in particular at higher resolutions. A possible reason for the discrepancies is due to the flow recirculation within the room [55]. Even if a similar environment has been realized, it is possible that the flow features within the room are different. Despite the difference at the second BPF, Fig. 6b shows that the discrepancies between the experiments and simulations at the first BPF and in terms of OSPL are within 1.5 dBA and 0.5 dBA respectively.

The above results suggest that the physical mechanisms are captured by the numerical simulations and give confidence that the comparisons described in the remaining of the paper are meaningful.

6. Results and discussion

6.1. Noise sources identification at free blowing conditions

The first step is the identification of the dominant noise sources at free blowing testing conditions ($\Delta p = 0\,Pa$). Numerical data from the semi-anechoic and free field computational domains are compared to assess the impact of the testing environment on the noise sources.

6.1.1. Aerodynamic results

First of all, it has been observed that changing the testing environment has an impact on the physical simulation time needed for reaching time convergence. Fig. 7 reports the time history, expressed in terms of fan revolutions, of the blades' loading; the mean value of the last 10 revolutions has been subtracted. The simulation in the semi-anechoic room converged after 10 revolutions, mainly because of the confined environment in which the flow is moving, while the two simulations in the free field domain needed approximately 30 revolutions to reach time convergence. The free field testing environment without the wall shows loading fluctuations with smaller amplitude with respect to the case in presence of the wall probably because of the different inflow patterns,
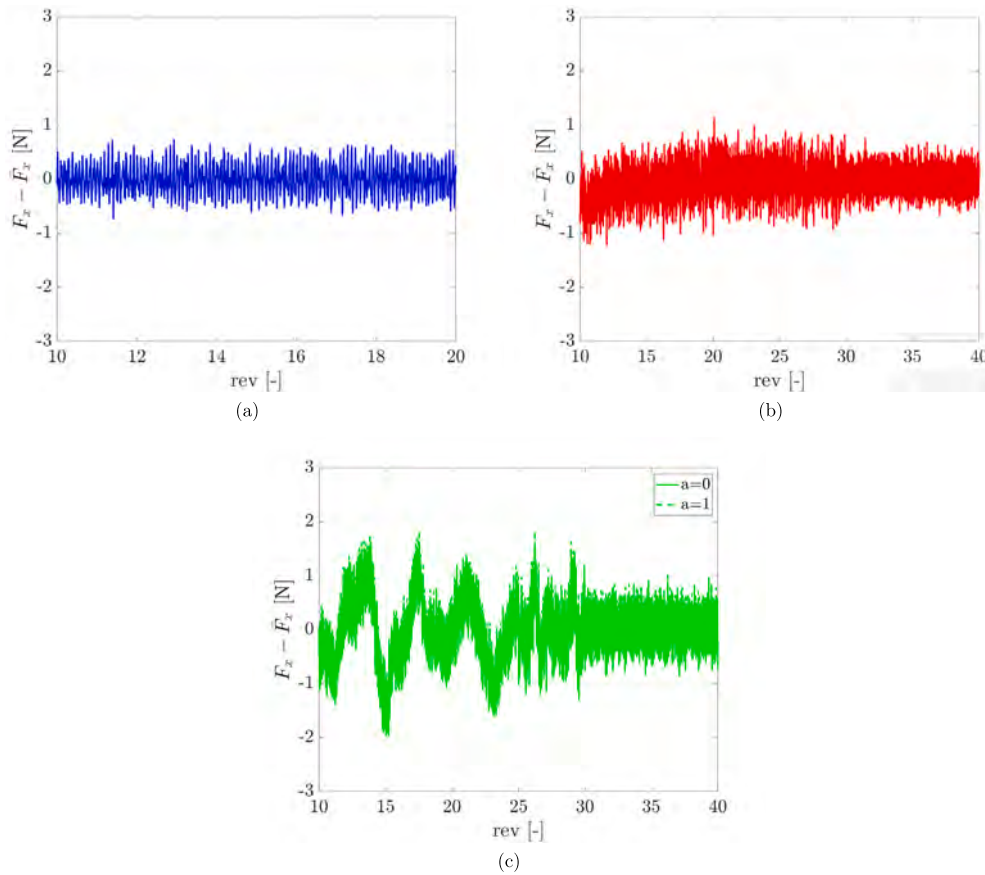
Fig. 7. Blades' loading fluctuations history for the three configurations at free blowing conditions. The fluctuations are defined with respect to the mean value of the signal over the last 10 revolutions. (a): Semi-anechoic. (b): Free field. (c): Free field - Wall.

Table 2
Aerodynamic integral quantities for the three testing environments at free blowing conditions. For each case, the mean value over the last 10 revolutions is shown.

	Semi-anechoic	Free field	Free field - Wall $(a = 0)$	Free field - Wall $(a = 1)$
$\dot{m}/\dot{m}_{Exp}$	0.987	0.991	1.091	1.089
Q/Q_{Exp}	1.045	1.045	0.910	0.908

as will be shown next. The fully reflective and fully absorbing wall cases do not show any difference in terms of loading and general flow topology. Therefore, if not mentioned explicitly, the fully absorbing case is not further reported when looking at the aerodynamic field.

The resulting mass flow rate and aerodynamic torque are reported in Table 2 as averaged values over the last 10 revolutions. The mass flow rate reported here is the one sampled on the plane at $x/D = 0$. Data obtained from other planes do not show significant differences. It can be noted that the presence of the semi-anechoic chamber, allowing for flow recirculation within the room, has a negligible effect on these quantities when compared with the free field testing environment; on the other hand, the introduction of the thin wall, needed to impose a pressure difference, results in a mass flow rate increase of about 10% and aerodynamic torque decrease of about 13% with respect to the free field testing environment. These differences can be explained by looking at the different inflow patterns between the two free field cases.

Fig. 8 shows the mean flow topology for the three simulated environments at $y/D = 0$. The figure shows the contours of the non-dimensional axial velocity component u/v_{tip}, where v_{tip} is the tip velocity, with superimposed streamlines. Data is obtained as a time average over the last 10 revolutions after time-convergence is reached. From the visual

inspection of the figure, it is clear that the presence of a confined environment (Fig. 8a) causes flow recirculation; consequently, the fan ingests flow from regions located downstream. Removing the anechoic walls, thus mimicking free field flow conditions (Fig. 8b), the flow recirculation disappears, and the vortices, developed in the wake of the fan, are convected downstream towards the outlet. Since the latter configuration required more revolutions to reach convergence, the wake is convected further downstream than for the other testing environment. Moreover, because the configuration with the wall is characterized by a higher mass flow rate, the wake vortices are convected further downstream, passing over the right boundary of Fig. 8c. By comparing the streamlines between the first two configurations, it is possible to conclude that the flow upstream of the fan will be subjected to a different distortion which can have an impact on the far-field noise. If the same fan is tested with the same conditions but with the presence of a wall (Fig. 8c) the upstream streamlines show a radial pattern. This will cause the increase in mass flow rate (Table 2) because the flow is forced to go through the fan. Moreover, the torque decrease is due to the reduction of the mean loading caused by the higher mass flow rate at this operating condition. The flow topology is the same for both walls analyzed. The differences in the streamline patterns can explain the differences in the mass flow rate reported above, as well as in the loading fluctuations amplitude between Fig. 7b and Fig. 7c.

In order to quantify the impact of the testing environment on the fan inflow velocity profile, the non-dimensional azimuth-averaged axial velocity profiles upstream of the fan ($x/D = -0.12$) are shown in Fig. 9. Results confirm previous qualitative observations: the presence of the wall alters the inflow pattern, thus causing an increase in mean axial velocity and of the mass flow rate through the fan. The removal of the semi-anechoic chamber does not show any relevant variation, except at the hub region ($r/R \leq 0.5$). It can be recognized a slight asymmetry
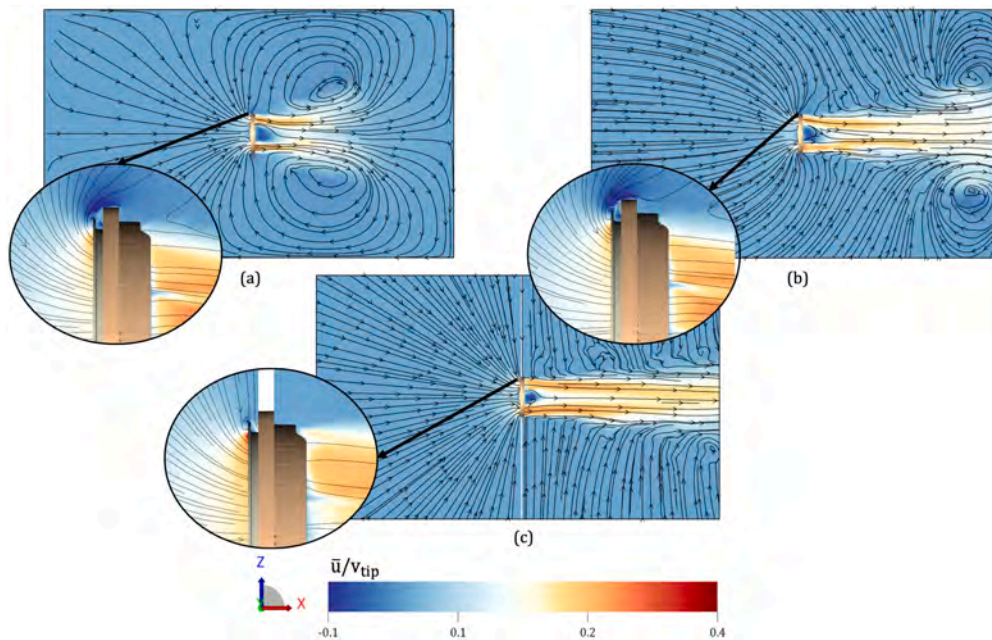
Fig. 8. Mean axial velocity in a plane located at $y/D = 0$ with streamlines. (a): Semi-anechoic. (b): Free field. (c): Free field - Wall.
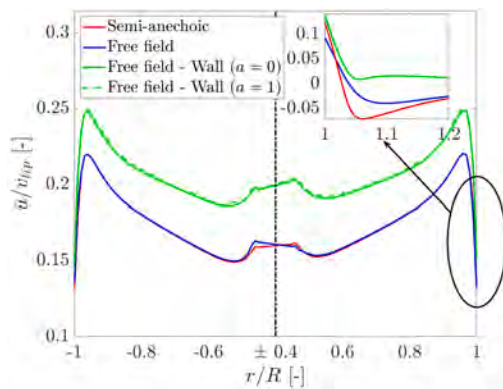

Fig. 9. Mean axial velocity profile upstream of the fan, at $x/D = -0.12$, at free blowing conditions, obtained as an azimuthal average of the signal. The range $r/R \leq 0.4$ has been removed from the x-axis of the graphs, in correspondence with the dash-dotted black line, because of the hub surface covering that radial range. The range $1 \leq r/R \leq 1.2$ is shown on the top-right side of the figure.

between the left and right sides of the figure, which is attributed to the presence of the honeycomb-like structure in the bottom-left area of the shroud (Fig. 1a). Focusing on the near-tip region ($1 \leq r/R \leq 1.2$), shown in the top-right corner of Fig. 9, it is possible to notice small amplitude reverse flow in both simulations without the thin wall probably due to the low-pressure area immediately upstream of the fan and the absence of any obstacles that could prevent the flow from moving backward. The amplitude of the negative axial velocity is larger for the semi-anechoic testing environment with respect to the free field one at $r/R = 1.05$, but both approach the same asymptotic value from $r/R = 1.2$. The free field domain is characterized by a more uniform velocity distribution, due to the absence of the large-scale vortices present in the semi-anechoic testing environment (Fig. 8a). Lastly, one can note that the thin wall inhibits the flow to return upstream of the fan, as outlined by the green line in Fig. 9. This can affect the amplitude of the velocity fluctuations near the tip region, and therefore, the blade loading fluctuations. As expected, the effect of the sound-absorbing coefficient of the thin wall on aerodynamic performances is almost negligible.

The upstream average flow characterization is completed by showing the turbulence intensity and integral length scale, computed at

Table 3
Turbulence intensity and integral length scale averaged on a circular plane of radius $r/R \leq 1.3$ located at $x/D = -0.12$ for the three testing environments at free blowing conditions.

	Semi-anechoic	Free field	Free field - Wall
Tu [%]	1.113	1.107	0.500
Λ/D [-]	0.121	0.122	0.099

$x/D = -0.12$ and $r/R \leq 1.3$, in Table 3. The free field environment is characterized by lower Tu and higher Λ with respect to the other cases. The presence of the wall results in an increase of Tu and decrease of Λ.

The analysis continues by investigating the interstage region between rotor blades and stator vanes because crucial for rotor-stator interaction. Fig. 10 shows the mean axial velocity field on a plane located at $x/D = -0.06$; the angle θ describes the angular position with $\theta = 0°$ coinciding with the z axis. It can be seen that the flow field is radially more uniform for the free field - wall testing environment case, while in absence of the wall, a more evident axial velocity decrease is found in the near hub region $r/R \leq 0.55$. Moreover, an area of lower velocity is present at $\theta = 200°$, caused by the presence of the honeycomb-like structure. It is expected that the presence of this structure can largely affect the blade loading and, therefore, the acoustic footprint of this fan.

To further characterize the flow field in this region, the instantaneous axial velocity field on a ring of radius $r/R = 0.82$ and the $\Lambda_2 = -10^8 \, 1/s$ isosurfaces in the fluid volume between rotor and stator are shown in Fig. 11. All three cases show flow separation on the blades' pressure side, occurring because the fan is operating in an off-design condition with zero pressure difference. The flow separation is more severe in the free field - wall testing environment. This is because the local angle of attack seen by the blades, in this condition, is higher than the design one. This is qualitatively visualized through the larger number of vortices in the fan blades' wake, which is wider and characterized by higher axial velocity values. The same figure shows the features of the flow impinging on the stator vanes, with a more chaotic flow for the free field - wall test. Flow separation is better shown in Fig. 12, where the instantaneous pressure coefficient distribution in the normalized chordwise direction is shown at two different θ locations, corresponding respectively to the blockage area ($\theta = 200°$) and to a phase in which the blade is facing a stator vane
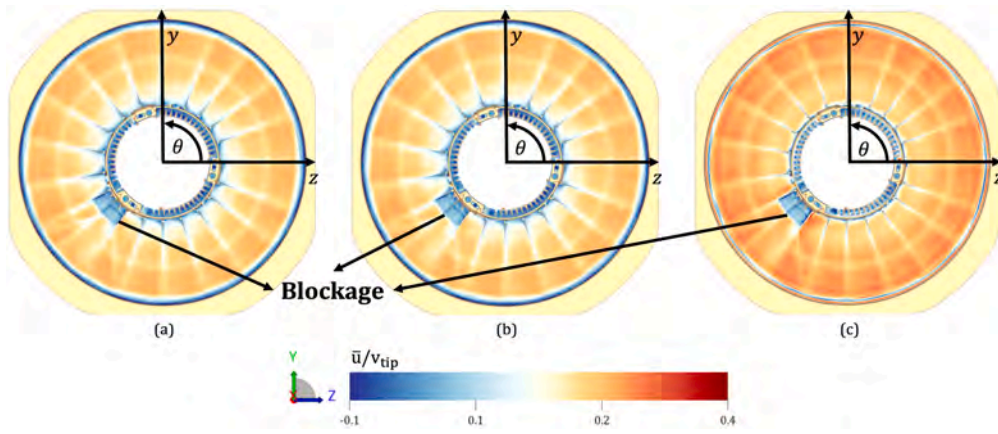
Fig. 10. Mean axial velocity in a plane located at $x/D = -0.06$. The fan has been removed from the visualization. (a): Semi-anechoic. (b): Free field. (c): Free field - Wall.
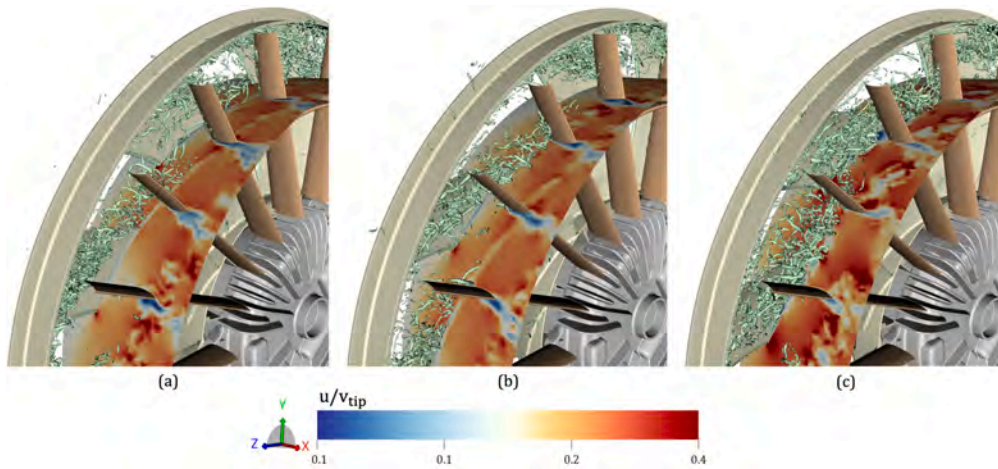

Fig. 11. Instantaneous axial velocity field on a ring of radius $r/R = 0.82$ and $\Lambda_2 = -10^8 \, 1/s$ isosurfaces in the fluid volume between rotor blades and stator vanes. (a): Semi-anechoic. (b): Free field. (c): Free field - Wall. The surface of the shroud and the wall have been removed from the visualization.
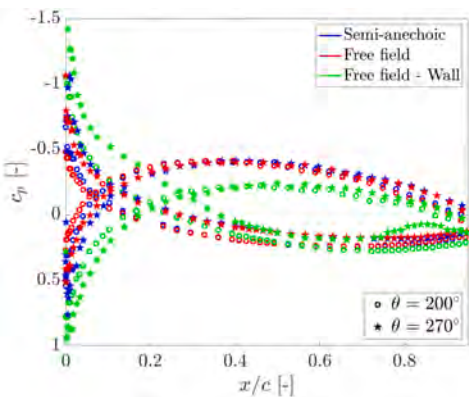

Fig. 12. Pressure coefficient on one blade at two different azimuthal angles θ. The angle $\theta = 200°$ corresponds to the lower axial velocity area seen in Fig. 10, while $\theta = 270°$ corresponds to the higher axial velocity area.
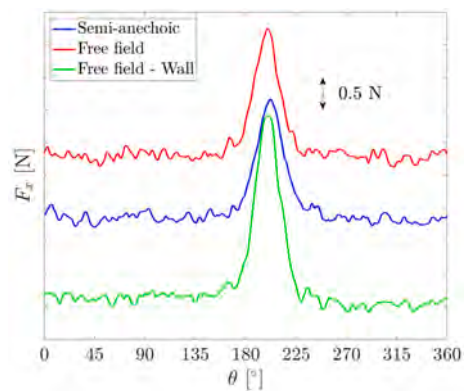

Fig. 13. Loading history of one blade over a rotation cycle at free blowing conditions.

($\theta = 270°$). The results confirm that, in all three cases, the flow over the blades is separated and that, at $\theta = 200°$, the area between the suction and pressure sides curve is higher, thus resulting in a loading hump. Moreover, for the free field - wall condition the inversion of the curves occurs further from the blade trailing edge.

Both the flow separation over the blades' pressure side and the flow blockage region at $\theta = 200°$ affect the time-history of the blade loading in the axial direction F_x shown as a function of θ in Fig. 13. As

expected, for all the configurations, F_x exhibits an evident hump at $\theta = 200°$, which corresponds to the location where the honeycomb-like structure is. This happens because of a potential effect of the structure that causes a change in inflow velocity and therefore of the angle of attack. It can be noted that the switch from the semi-anechoic chamber to the free field domain results in a slight loading increase, although the prominence of the loading hump remains unchanged. Conversely, when the thin wall is placed, the mean loading decreases due to the more severe flow separation over the blade, while the prominence of the hump
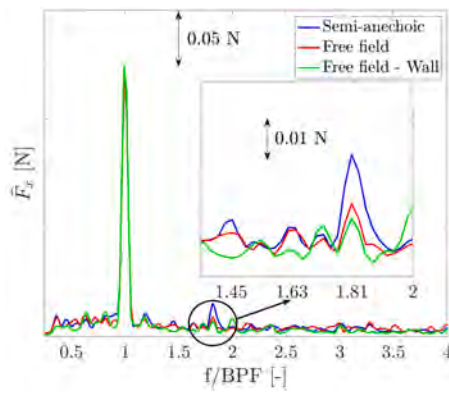
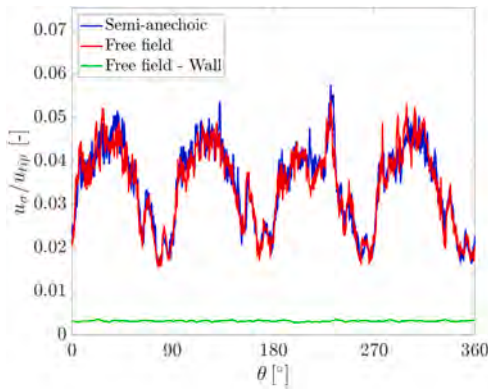**Fig. 14.** Spectrum of the loading given by all 11 blades at free blowing conditions.

Fig. 15. Distribution of the standard deviation of the axial velocity component at $x/D = -0.12$ and $r/R = 1.07$ for the free blowing condition.

increases. This is because the axial velocity component at $\theta = 200°$ is mostly the same in all cases.

The unsteady loading of the entire fan is analyzed in the frequency domain in Fig. 14, where the BPF is used to non-dimensionalize the frequency. The peak at the BPF is prominent in all the cases, especially when the thin wall is introduced in the free field domain, and it is due to the loading hump. In addition, a sub-harmonic hump is visible at $f/BPF = 1.81$ and is given by the interaction of the 11 blades with the 20 stator vanes; the interaction frequency is given by the ratio between the number of vanes and blades, i.e. $20/11 = 1.81$. This contribution is visible in the spectrum since the blades are not evenly spaced; therefore, other frequencies rather than the BPF and harmonics arise. Finally, another hump is present at $f/BPF = 0.35$, with a lower prominence in the free field - wall testing environment.

To better explain the last finding, the standard deviation of the axial velocity fluctuations u_σ is sampled at $x/D = -0.12$, over a circumference of radius $r/R = 1.07$ and shown in Fig. 15. Both semi-anechoic and free field testing environments show a periodicity with local maxima at $\theta = 45°, 135°, 225°, 315°$. This is due to the fact that the shroud is not circular; the four points correspond to the locations where the thickness of the shroud is the minimum. The 11 blades pass 4 times each at these locations, therefore, the loading will fluctuate at a frequency of $f/BPF = 4/11 = 0.35$. Conversely, when the thin wall is present, the axial velocity fluctuations are substantially absent because it has the effect of minimizing these variations.

6.1.2. Acoustic results

Fig. 16 shows the spectrum of the SPL of the acoustic pressure fluctuations sampled at $x/D = -2.15$, $y/D = z/D = 0$ in dBA. This location is chosen because relevant for industrial acoustic measurements.
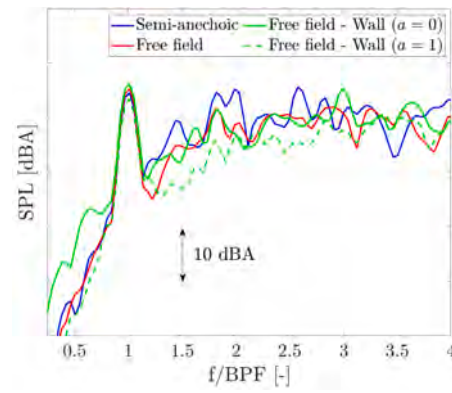

Fig. 16. Pressure fluctuations $2.15D$ upstream along the fan axis at free blowing conditions.

For all the testing conditions, spectra present expected features: a tone at the BPF, which weakly depends on the testing environment, i.e. the variation is within 1 dBA, and a broadband noise increase at higher frequencies with distinguishable tonal peaks with smaller prominence with respect to the one at the first BPF. The amplitude of the smaller peaks varies with the testing environment. Switching from the semi-anechoic to the free field environment, while the tone at $f/BPF = 1.81$ is always visible but with less amplitude, the one at the second BPF almost disappears. The free field configurations without the wall and with a fully reflective wall show similar behavior in the high-frequency range. The main difference is a small amplitude tone appearing at $f/BPF = 3$ when the fully reflective wall is present. It is interesting to notice that, if the wall is fully absorbing ($a = 1$), then noise decreases for $f/BPF > 1$. The overall SPL is reduced by 1.5 dBA when the semi-anechoic chamber is removed and further reduced by an additional 1 dBA when the wall is sound absorbing.

The higher noise found at frequencies higher than the BPF, when the semi-anechoic environment is considered, is caused by the flow recirculation as it was also found by Sturm et al. [32] when comparing their results with Zhu [56]. On the other hand, the tone at the BPF is less affected because it is due to the presence of the honeycomb-like structure.

To determine precisely which component of the fan is responsible for the far-field noise at the microphone of interest, the solid formulation of the FWH acoustic analogy is adopted and the results are shown in Fig. 17. The surfaces of the blades, hub, and ring are aggregated together into a single surface named as fan. Each sub-figure shows the contribution of each component (solid line) with respect to the overall far-field noise (dashed line). The contribution of the fan is shown in Fig. 17a, the one of the stator vanes in Fig. 17b, and the one of the shroud in Fig. 17c. It is evident that the fan is the most relevant contributor to the far-field noise being about 10 dBA higher than the others.

Comparing the testing environments, it is interesting to notice that the contributions to the far-field noise from stator vanes and the shroud are the ones most affected by the presence of the fully reflective wall. More in detail, in the presence of the fully reflective wall, the contribution of the stator vanes becomes about 5 dBA higher for $f/BPF > 1.5$, while the shroud shows higher noise at the 2nd and 3rd BPF. In this case, it is also interesting to notice that the fully reflective wall has also an impact on the noise radiated by the fan. As a matter of fact, the contribution of the fan component is higher than the noise obtained considering all components. This is due to acoustic reflections and, subsequent destructive interference.

After having identified the fan as a main contributor to the far-field noise, $Optyd\,B - pf\,noisescan$ is used to detect the time-averaged contribution of each surface element to the far-field noise in dB/m^2 for all the investigated testing environments. Two frequencies are analyzed: the 1st (Fig. 18) and the 2nd BPF (Fig. 19). In each row of the figures, both the front and rear views of the fan are reported for the three configurations. A higher value of dB/m^2 in a certain area indicates a higher
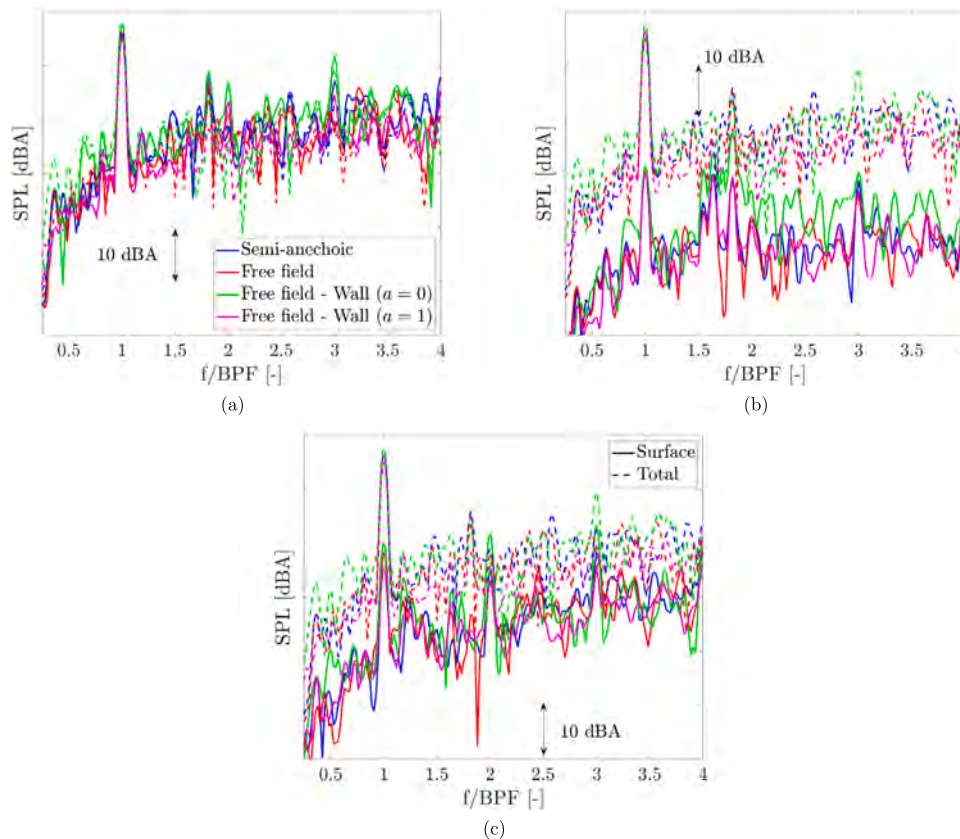
Fig. 17. Acoustic contribution of each main solid surface (solid line) $2.15D$ upstream at the probe aligned with the fan axis at free blowing conditions; it has been superimposed the total contribution (dashed line) of the entire simulated system on each plot. (a): Fan (blades + ring + hub). (b): Stator vanes. (c): Shroud.

contribution of that area to the microphone located at $x/D = -2.15$, $y/D = z/D = 0$, over the entire sampling period. The figures show only the surface contribution of the fan, while the stator vane surfaces have been displayed as a reference and colored green.

Fig. 18 shows the dB/m^2 map of the fan surface for the four configurations at free blowing conditions at $f/BPF = 1$. It can be recognized that the main noise contribution comes from the blades' pressure side (Fig. 18b, 18d, 18f, 18h). This is due to the presence of the honeycomb-like structure as described above. Since the dB/m^2 map in the figure indicates a mean over the sampling period, the contribution is present on every blade. Videos attached as supplementary material show the largest contribution of the blades passing in front of the honeycomb-like structure area. The presence of the thin wall (Fig. 18e, 18f) increases the contribution from the pressure side. This is because of the wider flow separation area over the blades. The massive flow separation over the blades that affects the configuration with the thin wall might also be responsible for the slightly higher contribution at the trailing edge, in the hub region, that is visible in Fig. 18e when compared to Fig. 18a and 18c. Moreover, it is seen a decrease in the ring surface contribution in Fig. 18e with respect to Fig. 18a and 18c. This can be attributed to the strongly reduced flow recirculation from downstream, which prevents the ring from experiencing strong wall pressure fluctuations. Finally, the fully absorbing wall in Fig. 18g, 18h has a beneficial effect compared to the fully reflecting one in Fig. 18e, 18f. This can be attributed to the different interference pattern between the fan and wall surfaces within the two different absorbing properties of the thin wall.

Fig. 19 shows the dB/m^2 map of the fan surface for the four configurations at free blowing conditions at $f/BPF = 2$. There are noteworthy differences in amplitude on the blades' suction side (Fig. 19a, 19c): the higher intensity inflow velocity fluctuations in the semi-anechoic room with respect to the free field domain causes regions with high amplitude noise sources. Moreover, the noise sources distribution on the blades'

pressure side in Fig. 19b and 19d show two interesting features: the first is an increase of noise in the tip area; the second is that each time a blade passes in front of a stator, there are two regions that contribute largely to the noise, thus suggesting that the solidity and shape of the stator vanes has a potential effect on the loading, even if not very visible from the aerodynamic observations. These aspects will be discussed in more details in the next section. The introduction of the thin wall (Fig. 19e, f) further reduces the noise contribution on the blades' suction side; this can be attributed to the reduction of inflow fluctuations. The contribution on the pressure side is, conversely, enhanced. Lastly, the fully absorbing wall (Fig. 19g, h) has a beneficial effect on the source amplitude, while not changing significantly the pattern.

6.2. Operating condition effects

The variations of the flow field and far-field noise with the operating condition are assessed by comparing the free blowing and maximum efficiency cases in the free field domain. The thin wall, either fully reflective or fully absorbing, is always present because it is needed in any experimental facility to impose a pressure difference. Starting from this paragraph, the configuration at free blowing conditions in the free field domain with the thin wall is named "free blowing", while the maximum efficiency one is named "max efficiency".

6.2.1. Aerodynamic results

The results of this paragraph will be presented only for the fully reflecting case because of the negligible differences on the aerodynamics described in the previous section.

The first analysis is the assessment of the time convergence of the solution for the two operating conditions. Fig. 20 reports the time history of the blades' loading minus the mean value of the last 10 revolutions. Also in this case, 30 revolutions were necessary to reach time conver-
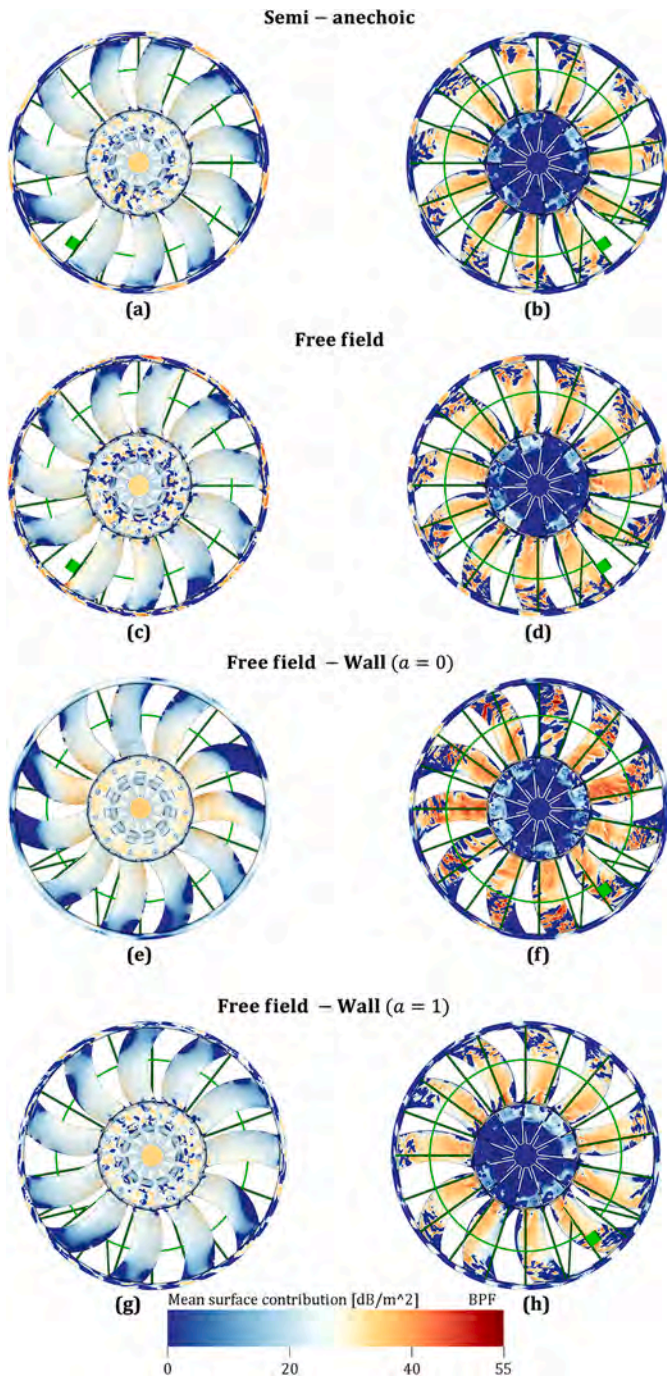
Fig. 18. Surface noise contribution at the probe $x/D = -2.15$, $y/D = z/D = 0$ and at $f/BPF = 1$ under free blowing conditions. (a, b): Semi-anechoic. (c, d): Free field. (e, f): Free field - Wall ($a = 0$). (g, h): Free field - Wall ($a = 1$).

Fig. 19. Surface noise contribution at the probe $x/D = -2.15$, $y/D = z/D = 0$ and at $f/BPF = 2$ under free blowing conditions. (a, b): Semi-anechoic. (c, d): Free field. (e, f): Free field - Wall ($a = 0$). (g, h): Free field - Wall ($a = 1$).

gence. Finally, it has also been verified that the wake downstream of the fan is sufficiently developed.

The averaged mass flow rate on the plane at $x/D = 0$ and the torque are reported in Table 4 made dimensionless using the experimental values at free blowing provided by the manufacturer. The reference experimental values are the same so that the comparison between the two operating points can be made. When the fan operates at maximum efficiency the mass flow rate decreases by about 50% while the aerodynamic torque increases by about 55% compared with the free blowing conditions. Indeed, the higher loading to which the blades are subjected, due to the presence of a pressure difference, also results in an increase in torque.
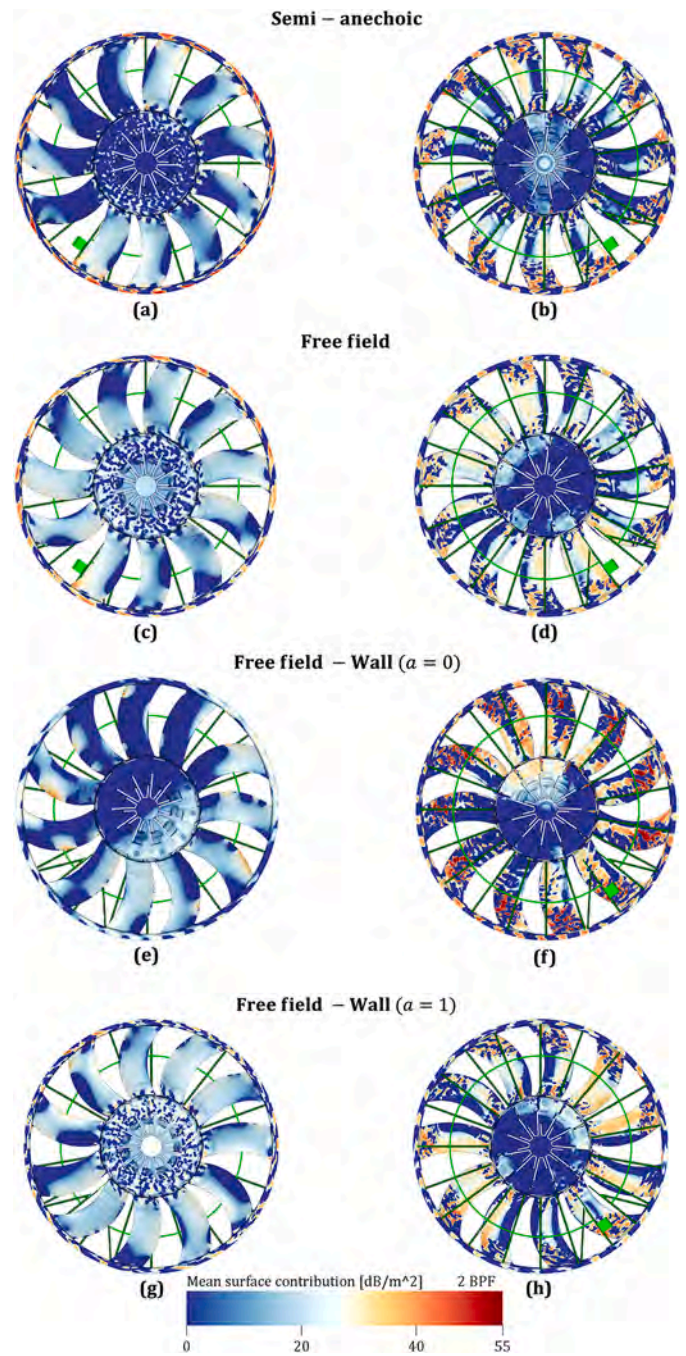
Table 4
Non-dimensional mass flow rate and torque. The ratio between numerical and experimental results is shown.

	Free blowing	Max efficiency
$\dot{m}/\dot{m}_{Exp}$	1.091	0.541
Q/Q_{Exp}	0.910	1.418

The flow topology near the fan is shown in Fig. 21. In the figure, the contour of the non-dimensional time-averaged velocity component and streamlines are shown in a square region of $2.15D \times 2.15D$ at $y/D = 0$. It can be noted that the higher mass flow rate at free blowing operat-
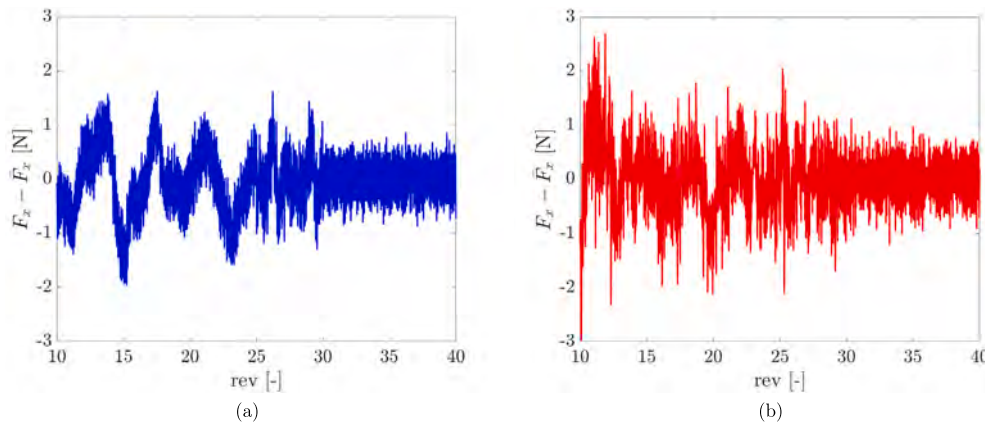
Fig. 20. Blades' loading fluctuations history for the free blowing and maximum efficiency conditions in the free field testing environment with the wall. The force time-averaged value over the last 10 revolutions is subtracted. (a): Free blowing. (b): Max efficiency.
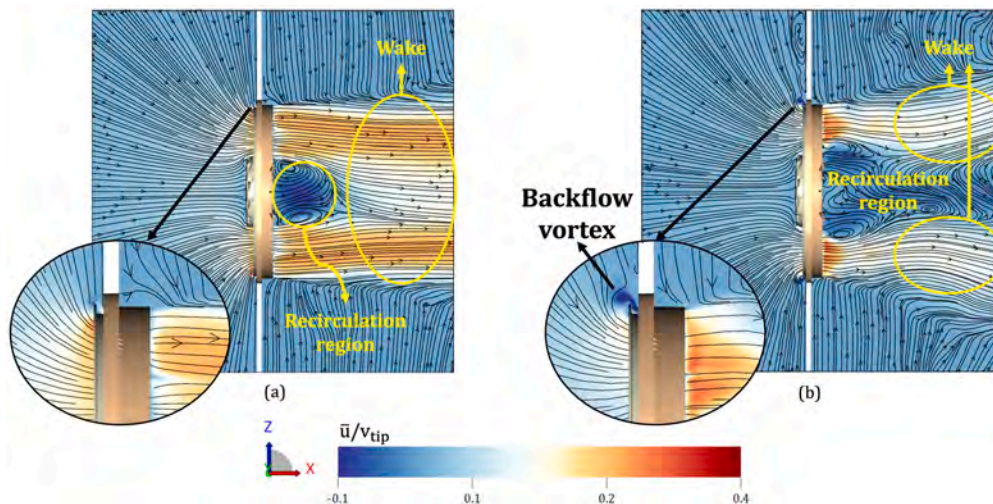

Fig. 21. Contours of the time-averaged axial velocity with superimposed streamlines at $y/D = 0$. (a): Free blowing. (b): Max efficiency.

ing point (Fig. 21a) causes a wake with higher velocity with respect to the maximum efficiency setting. For the latter case, the recirculation region behind the engine (Fig. 21b) is substantially larger. This is because, in the near wake, the two high-speed wakes do not merge. This phenomenon is typical when dealing with a nonzero pressure difference across the fan, as reported by Kim et al. [57].

A major difference between the two testing conditions is the appearance of a back-flow, happening in the gap between the shroud and the ring, at maximum efficiency (Fig. 21b). The back-flow is re-ingested by the blades, as previously shown by Magne et al. [9]. This is known to be a cause of unsteady loading noise and will be discussed in the next section.

To further quantify the differences between the two testing conditions, the time and azimuth averaged axial velocity profile upstream of the blades is shown in Fig. 22 at $x/D = -0.12$ in the range from $0.4 < r/R < 1$. For clarity, the hub $r/R \leq 0.4$ has been removed while a zoom of the near tip region $1 \leq r/R \leq 1.2$ is shown in the top-right corner. As expected, the maximum efficiency configuration is characterized by a lower time-averaged axial velocity over the entire radial extension and by a steeper decrease in the proximity of the hub region. Moreover, for the maximum efficiency configuration, the back-flow is evident and extends in the range $1.03 < r/R < 1.12$, thus resulting in a vortex characterized by a length scale of about 10% of the radius.

Finally, the turbulence intensity and integral length scale at $x/D = -0.12$ and $r/R \leq 1.3$ are reported in Table 5, showing that the maximum efficiency condition has both higher Tu and Λ.
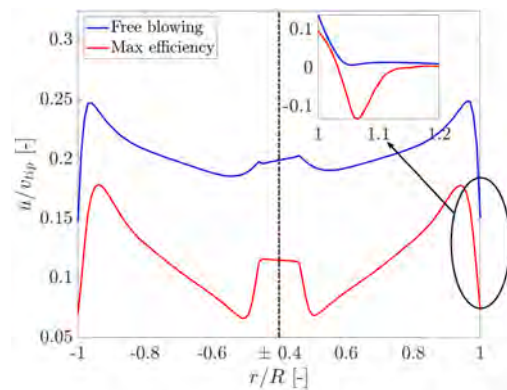

Fig. 22. Time and azimuth averaged axial velocity profile upstream of the blades is shown in Fig. 22 at $x/D = -0.12$ in the range from $0.4 < r/R < 1$. The hub $r/R \leq 0.4$ is removed while the near tip region $1 \leq r/R \leq 1.2$ is shown in the top-right corner.

As done previously, the interstage region is analyzed. Fig. 23 shows the time-averaged axial velocity in the yz plane located at $x/D = -0.06$ for the two different operating conditions. The effect of a substantially lower inflow velocity for the maximum efficiency operating point results in a less uniform flow pattern in the azimuth (Fig. 23b), unlike the free blowing condition (Fig. 23a). As a matter of fact, regions with evident local minima and maxima, corresponding to the stator vanes'
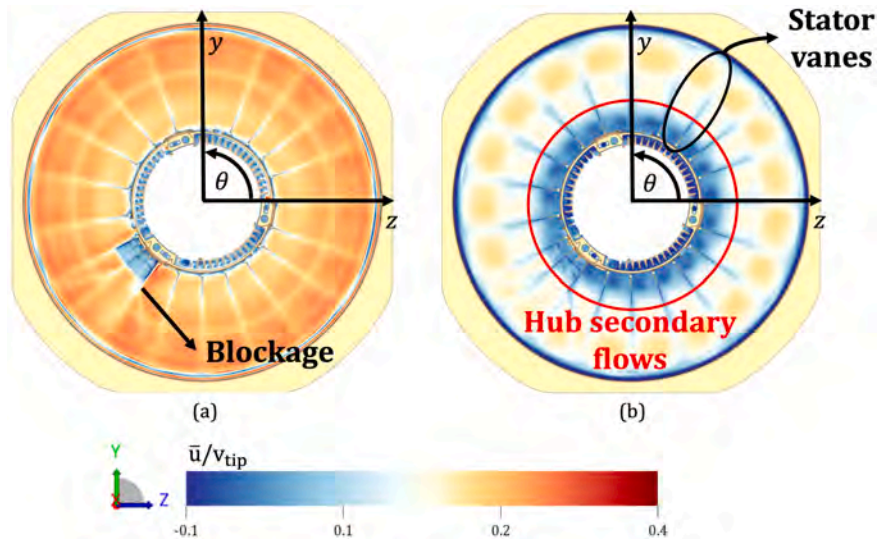
Fig. 23. Time-averaged axial velocity at $x/D = -0.06$ in the free field testing environment. (a): Free blowing. (b): Max efficiency.
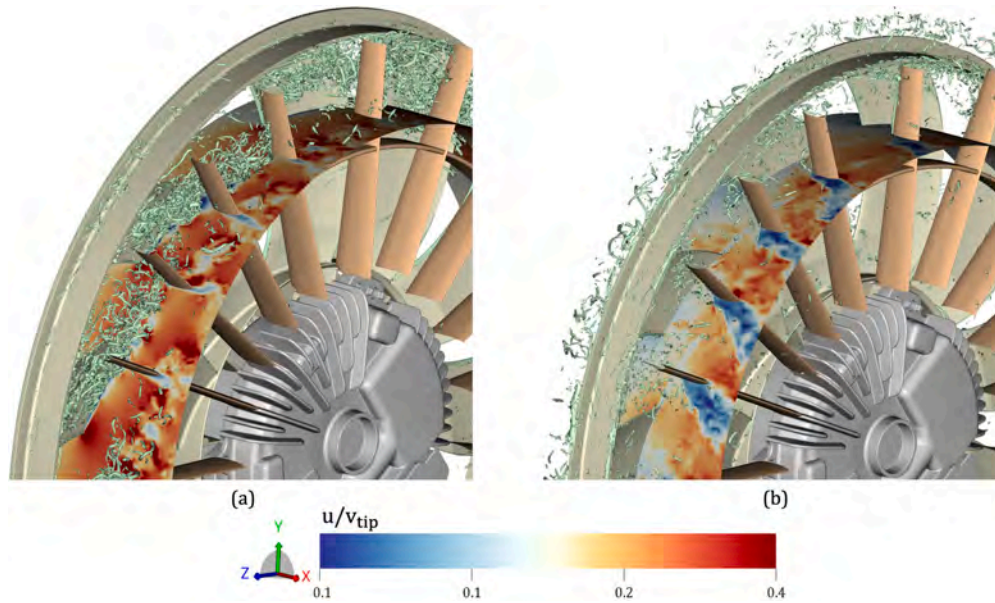

Fig. 24. Instantaneous axial velocity field on a ring of radius $r/R = 0.82$ and $\Lambda_2 = -10^8\ 1/s$ isosurfaces in the fluid volume between rotor blades and stator vanes in the free field. (a): Free blowing. (b): Max efficiency. The shroud and wall have been removed from the visualization.

Table 5
Turbulence intensity and integral length scale averaged on a circular plane of radius $r/R \leq 1.3$ located at $x/D = -0.12$.

	Free blowing	Max efficiency
Tu [%]	0.500	1.196
Λ/D [-]	0.099	0.601

locations, are visible. Because of the lower velocity, also the impact of the honeycomb-like structure, at $\theta = 200°$, is less strong. However, for the maximum efficiency condition, very close to the hub, the figure shows regions with localized negative $\bar{u}/v_{tip}$, thus confirming the presence of local flow recirculation. It can be concluded that, at maximum efficiency, the disturbance induced by the stator vanes is stronger with respect to the free blowing condition. This can have an impact on the periodic interaction between blades and vanes, both of potential and viscous nature, resulting in different fluctuation peaks both on blade loading.
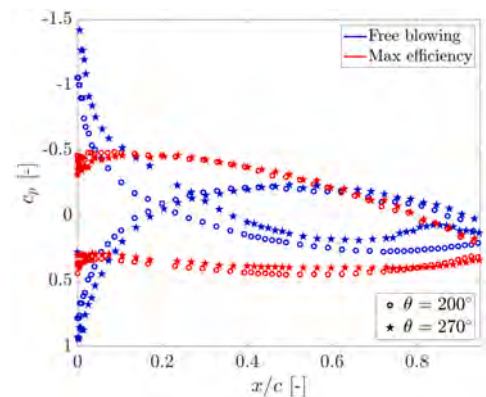

Fig. 25. Pressure coefficient on one blade at two different azimuthal angles θ. The angle $\theta = 200°$ corresponds to lower axial velocity area seen in Fig. 23a.
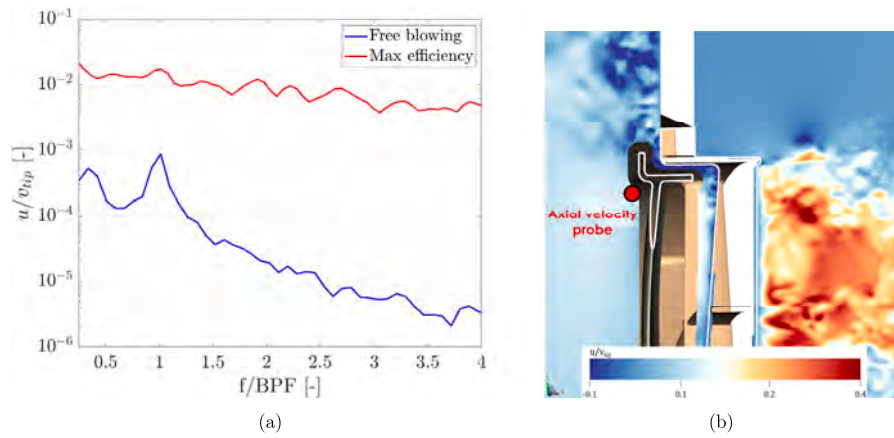
Fig. 26. Axial velocity fluctuations in the near tip-gap region at $x/D = -0.13$, $y/D = 0.54$ and $z/D = 0$), for the free blowing and maximum efficiency operating points in the free field testing condition. (a): Spectrum. (b): Probe location.
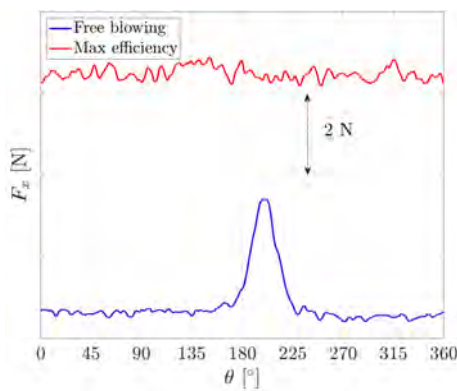

Fig. 27. Loading time-history of one blade over a rotation cycle, for the free blowing and maximum efficiency operating points in the free field setting.
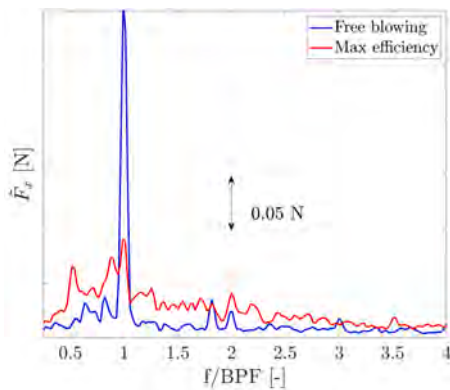

Fig. 28. Spectrum of the axial loading from all 11 blades, for the free blowing and maximum efficiency operating points in the free field setting.

Fig. 29. Spectra of the pressure fluctuations $2.15D$ upstream of the fan at the probe aligned with the fan axis of rotation. Both the free blowing and maximum efficiency operating points are shown with both reflecting ($a = 0$) and sound-absorbing ($a = 1$) thin wall.

The instantaneous flow field, in the rotor-stator gap and in the near-tip regions, is further investigated. Both the instantaneous axial velocity field on a ring of radius $r/R = 0.82$ and $\Lambda_2 = -10^8 \; 1/s$ isosurfaces in the fluid volume between rotor and stator are shown in Fig. 24. The free blowing and maximum efficiency operating conditions are shown in sub-figures (a) and (b), respectively, it is possible to notice that there are fewer vortical structures when the fan operates at maximum efficiency, thus suggesting that, as expected, the flow over the blades is attached because of the lower inflow velocity. This affects the interaction with the stator vanes. As a matter of fact, near the stator vanes more chaotic wakes are visible. Another relevant consideration is the absence
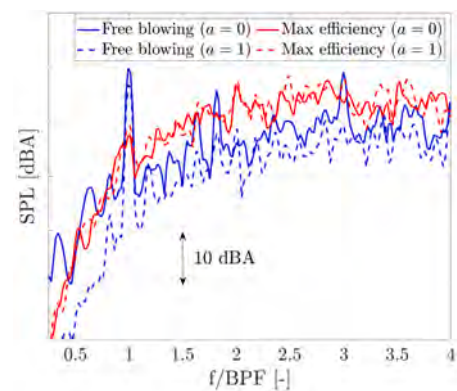
of vortices in the upper part of the ring for the free blowing case with respect to the maximum efficiency one. This supports the previous observations of vortices shed on the blade surfaces through the tip gap.

The pressure coefficient distribution is shown in Fig. 25 for the same two θ phases of the previous section. As expected, the maximum efficiency condition is characterized by an attached flow over the blades, as well as drastically lower variations between the two θ phases.

To characterize the flow through the tip gap, spectra of the axial velocity component for both configurations are shown in Fig. 26a. The fluctuations are sampled at $z/D = 0$, $x/D = -0.13$, and $y/D = 0.54$, as shown in Fig. 26b. The results confirm that at the maximum efficiency operating point, there are fluctuations with a higher amplitude that are broadband in nature, i.e., which are not a consequence of the local passage of the blades, contrary to the free blowing case. The latter is characterized by lower amplitude spectral content and two tonal peaks at $f/BPF = 0.35$, due to the fact that the shroud is not azimuthally uniform, and at $f/BPF = 1$ due to the passage of the blade. From an aeroacoustic perspective, it can be expected that the contribution to the far-field noise of the flow through the gap is more relevant at maximum efficiency.

Fig. 27 shows the instantaneous loading time-history of one blade over a rotation cycle for both configurations. Data shows that, at maximum efficiency, the peak in loading at $\theta = 200°$ is not evident anymore but, as a consequence of the more relevant back-flow, the amplitude of the fluctuations is larger and uniform in the azimuth.

Spectra of the axial loading component of the entire set of blades are shown in Fig. 28 for the two operating points. The maximum effi-
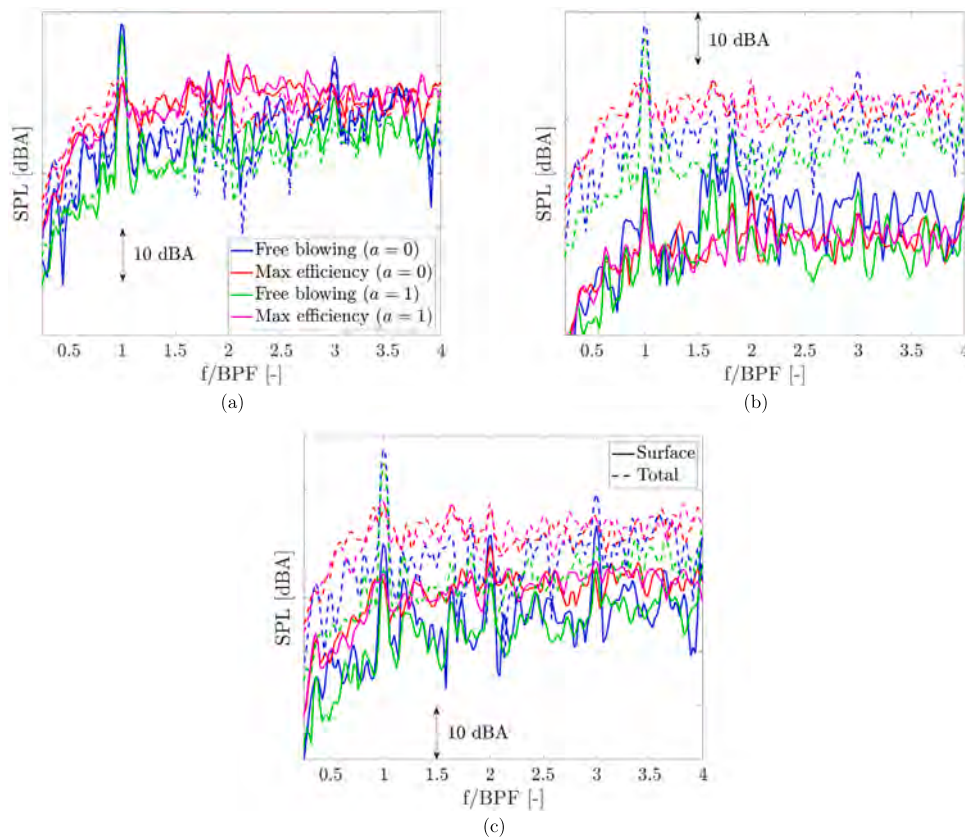
Fig. 30. Acoustic contribution of each solid surface (solid line) with respect to the overall noise. Virtual probe located $2.15D$ upstream along the fan axis of rotation. Both free blowing and maximum efficiency operating points in the free field are shown with reflective and sound-absorbing walls. (a): Fan (blades + ring + hub). (b): Stator vanes. (c): Shroud.

ciency condition is characterized by higher fluctuations in amplitude on a broad range of frequencies and a smaller peak at the BPF. The higher broadband fluctuations at maximum efficiency hide the smaller peak at $f/BPF = 1.81$ as well as the other inter-harmonic peaks that characterize the free blowing configuration.

6.2.2. Acoustic results

The results of this paragraph will include the configuration with the fully absorbing wall, since it has been previously shown that the differences on the acoustics are not negligible.

Fig. 29 shows the spectrum of the pressure fluctuations sampled at $x/D = -2.15$, $y/D = z/D = 0$, which corresponds to the upstream location along the fan axis, for the two operating conditions and for the two types of thin wall. Pressure has been sampled for the last 10 revolutions of the fan. The spectral content of the signals has been computed consistently with the previous acoustic analysis in section 6.1. The maximum efficiency operating condition is characterized by a strong reduction of the BPF tones at $f/BPF = 1$. The reduction in SPL is about 11 dBA, while the broadband content increases. This results in an increase of the overall SPL of about 2 dBA. At $f/BPF = 2$, the maximum efficiency configuration shows a prominent increase of SPL by 9 dBA, not evident in the free blowing case. This aspect will be investigated in the following. Lastly, the sound absorption property of the thin wall has more impact when the fan is operated at free blowing operating condition with respect to the maximum efficiency one. These differences are due to the fact that the acoustic radiation patterns are different and, therefore, there is a different impact of the acoustic reflections on the thin wall.

As done previously, the contribution of each component at the front virtual microphone is analyzed in Fig. 30. More in detail, the contribution of the fan is shown in Fig. 30a, the one of the stator vanes in Fig. 30b and of the shroud in Fig. 30c. Noise obtained from the direct

probe is shown as a continuous line. As for the previous comparisons, the fan (Fig. 30a) is responsible for most of the generated noise along the fan axis, thus reinforcing the conclusion that these low-speed axial fans are mainly dominated by the unsteady loading noise resulting from the interaction of the blades with a non-uniform and unsteady flow field. In addition, at maximum efficiency the noise caused by the fan is higher than the total one. In this case, the difference with respect to the overall measurement is even higher with respect to the free blowing case. As reported in section 6.1, this behavior is indicative of a destructive interference pattern taking place between the fan and the thin wall. Therefore, in the presence of a pressure difference across the wall, this interference is even more pronounced. The stator vanes contribution (Fig. 30b) shows interesting differences when comparing the different cases. At free blowing conditions there is an increase of tonal peaks at the BPF and at frequencies not multiple of the BPF, i.e. $f/BPF = 1.6$ and 1.81 with respect to the maximum efficiency operating condition. By introducing a sound-absorbing wall, there is a reduction of the noise intensity for $f/BPF > 1.5$. Conversely, the maximum efficiency condition does not show any relevant impact of the wall type and presents only an increase of the tonal peak at $f/BPF = 2$. The amplification of the tones at $f/BPF = 1.81$ for the free blowing case can be attributed to the larger loading fluctuations. Lastly, the shroud surface (Fig. 30c) at maximum efficiency is characterized by a higher broadband level on the entire frequency range, mainly due to the higher wall pressure fluctuations caused by the increased back-flow in the tip-gap region, delimited by the rotating ring and the shroud itself. The sound-absorbing property of the wall has a negligible impact on the far-field noise at max efficiency.

To investigate more in detail the differences in the noise sources distribution under the two different operating conditions, the time-averaged dB/m^2 maps at $f/BPF = 1$ (Fig. 31) and $f/BPF = 2$
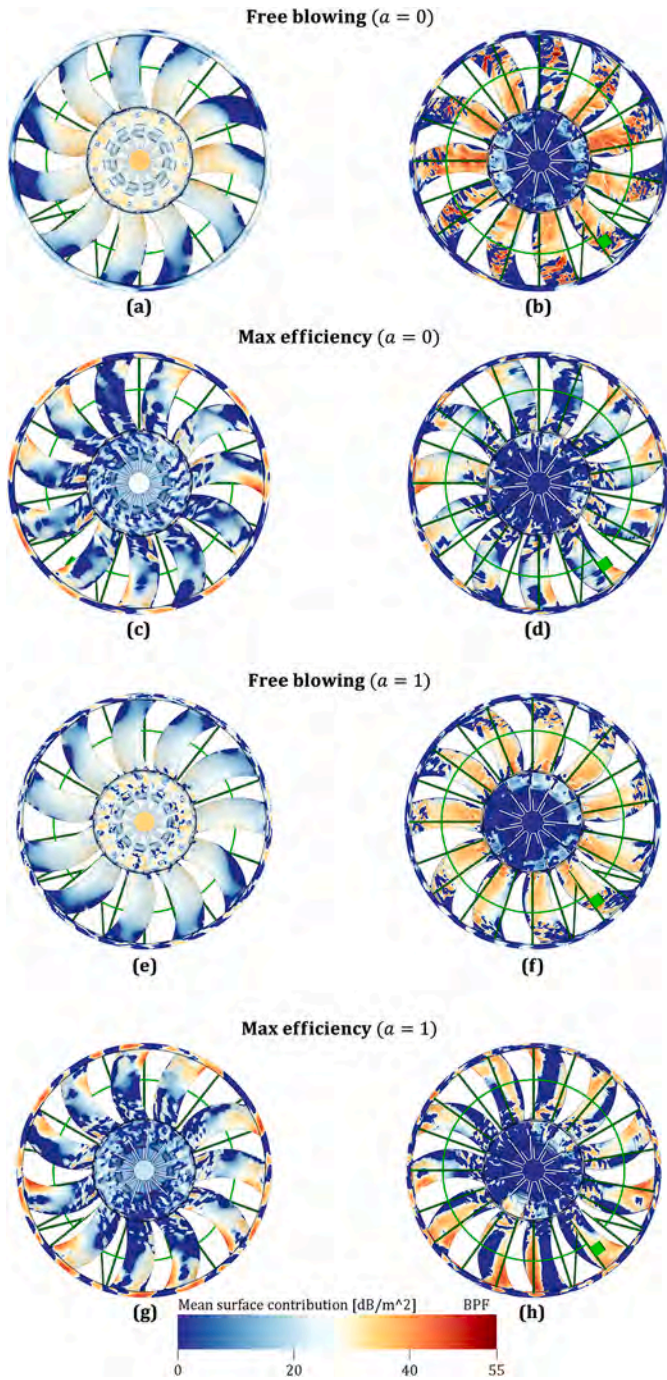
Fig. 31. Surface noise contribution at the probe $x/D = -2.15$, $y/D = z/D = 0$ and at $f/BPF = 1$, for the free blowing and maximum efficiency operating points in the free field. (a, b): Free blowing ($a = 0$). (c, d): Max efficiency ($a = 0$). (e, f): Free blowing ($a = 1$). (g, h): Max efficiency ($a = 1$).

Fig. 32. Surface noise contribution at the probe $x/D = -2.15$, $y/D = z/D = 0$ and at $f/BPF = 2$, for the free blowing and maximum efficiency operating points in the free field. (a, b): Free blowing ($a = 0$). (c, d): Max efficiency ($a = 0$). (e, f): Free blowing ($a = 1$). (g, h): Max efficiency ($a = 1$).

(Fig. 32) are shown consistently with what has been shown in section 6.1. The main contributions at the BPF (Fig. 31) for the free blowing configuration (Fig. 31a, 31b) are located on the blades' pressure side (Fig. 31 b), as a consequence of the interaction between the blades and the honeycomb-like structure area. For the maximum efficiency case (Fig. 31c, 31d), instead, the main contributions are located on the tip leading edge of the blades and the corresponding ring regions (Fig. 31c), which is indicative that the interaction of the back-flow vortex with the blade tips and the ring surfaces is the main source of noise at the BPF. The differences between the fully reflecting (Fig. 31a, 31b, 31c, 31d)
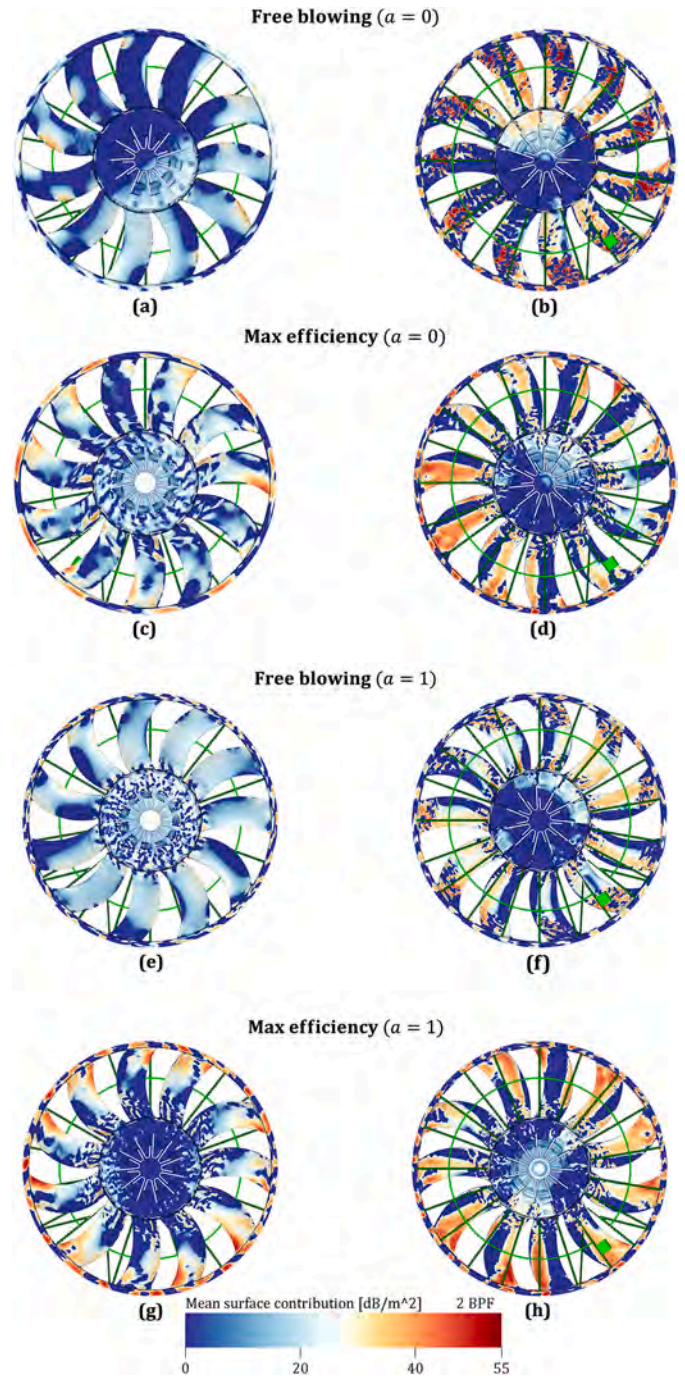
and the fully absorbing (Fig. 31e, 31f, 31g, 31h) walls are consistent with the previous discussions.

At $f/BPF = 2$ (Fig. 32), it is seen that the predominant source for both operating points is located at the blade pressure side. Since these higher amplitude regions are aligned with the stator vane positions, it can be inferred that rotor-stator interaction phenomena are dominant, with the low-order acoustic mode being excited at this frequency. Further contributions of the ring and both tip leading and trailing edges are seen only at maximum efficiency (Fig. 32c, 32d), which can be attributed to the interaction of those surfaces with the upstream back-flow

vortex. The effects of the wall sound absorption (Fig. 32e, 32f, 32g, 32h) are again in line with the results shown in the previous paragraphs.

7. Conclusions

This study reports a comprehensive numerical investigation of how the measurement settings impact the far-field noise measured when testing an industrial engine cooling fan. Two operating conditions are investigated. For this scope, for tests at free blowing conditions, a conventional test in a semi-anechoic room is compared against an ideal free field testing environment and an environment where a wall is placed as in an ideal anechoic aeraulic facility. The separating wall is modeled as fully reflective and fully sound absorbing.

In the semi-anechoic chamber at free blowing conditions, the predominant noise source is related to a localized flow blockage due to the presence of honeycomb-like structure, which alters the blade loading, resulting in a tonal peak in the far-field noise spectra at the blade passing frequency. In this condition, the flow over the blades is mainly separated. When the semi-anechoic chamber is removed, transitioning to a free field environment, it has been observed a reduction in the harmonics of the blade passing frequency in the far-field acoustic spectra, as well as in a few of the sub-harmonic humps. This reduction is attributed to the absence of recirculation, emphasizing the significance of environmental conditions on noise generation. The placement of a thin wall increases the mass flow rate through the impeller, resulting in a more severe flow separation over the blades and, therefore, a higher amplitude on the blade loading fluctuation, thus increasing the noise generated. The wall substantially reduces the flow recirculation between downstream and upstream, with a subsequent drop of the blade loading hump at $f/BPF = 0.35$. Finally, the effects of a fully absorbing wall against a fully reflecting one are almost negligible on the flow field, while are substantial on the far-field acoustics.

At the fan maximum efficiency point, where a pressure difference across the fan is introduced, the generation of a stationary recirculation vortex in the fan's ring region became the main noise generation mechanism. The vortices interact with the blade tip leading edges, resulting in an acoustic spectrum showing a higher broadband content on all the frequencies of interest and a lower tone at the BPF. This is enhanced by the flow distribution over the blade, which is mostly attached, with a subsequent change in the unsteady loading time variation. The SPL drop given by the transition from a reflecting thin wall to an absorbing one is more evident in the off-design configuration (free blowing), as a result of a different sound radiation pattern compared with the on-design case (maximum efficiency). In addition, a tone at the BPF's first harmonic is seen.

CRediT authorship contribution statement

Francesco Bellelli: Writing – original draft, Visualization, Validation, Investigation, Formal analysis, Data curation, Conceptualization. **Renzo Arina:** Writing – review & editing, Supervision, Resources. **Francesco Avallone:** Writing – review & editing, Supervision, Resources.

Declaration of competing interest

The authors declare that they have no known competing financial interests or personal relationships that could have appeared to influence the work reported in this paper.

Data availability

The data that has been used is confidential.

Appendix A. Supplementary material

Supplementary material related to this article can be found online at https://doi.org/10.1016/j.apacoust.2024.110252.

References

[1] Sharland IJ. Sources of noise in axial flow fans. J Sound Vib 1964;1(3):302–22.

[2] Moreau S. The third golden age of aeroacoustics. Phys Fluids 2022;34(3):031301.

[3] Piwowarski M, Jakowski D. Areas of fan research—a review of the literature in terms of improving operating efficiency and reducing noise emissions. Energies 2023;16(3):1042.

[4] Zhou W, Zhou P, Xiang C, Wang Y, Mou J, Cui J. A review of bionic structures in control of aerodynamic noise of centrifugal fans. Energies 2023;16(11):4331.

[5] Brooks TF, Pope DS, Marcolini MA. Airfoil self-noise and prediction. Tech. Rep., NASA. 1989.

[6] Díaz AKM, Fernández OJM, Marigorta EB, Morros CS. Numerical prediction of tonal noise generation in an inlet vaned low-speed axial fan using a hybrid aeroacoustic approach. Proc Inst Mech Eng, Part C 2009;223(9):2081–98.

[7] Yoshida K, Semura J, Kohri I, Kato Y. Reduction of the BPF noise radiated from an engine cooling fan. SAE technical paper series. SAE International; 2014.

[8] Cattanei A, Zecchin F Mazzocut, Di Pasquali A, Lazari A. Effect of the uneven blade spacing on the noise annoyance of axial-flow fans and side channel blowers. Appl Acoust 2021;177(107924):107924.

[9] Magne S, Moreau S, Berry A. Subharmonic tonal noise from backflow vortices radiated by a low-speed ring fan in uniform inlet flow. J Acoust Soc Am 2015;137(1):228–37.

[10] Sun Z, Tian J, Zhang T, Du Z, Ouyang H. Cooling fan aerodynamic noise reduction with short inlet duct and its applicability. Int J Refrig 2023;148:117–30.

[11] Ocker C, Geyer TF, Czwielong F, Krömer F, Pannert W, Merkel M, et al. Permeable leading edges for airfoil and fan noise reduction in disturbed inflow. AIAA J 2021;59(12):4969–86.

[12] Chaitanya P, Joseph P. Slitted leading edge profiles for the reduction of turbulence-aerofoil interaction noise. J Acoust Soc Am 2018;143(6):3494.

[13] Ocker C, Czwielong F, Chaitanya P, Pannert W, Becker S. Aerodynamic and aeroacoustic properties of axial fan blades with slitted leading edges. Acta Acust 2022;6:48.

[14] Peng Z, Wu Y, Tian J, Ouyang H. Discrete noise control of cooling fan module: stator and rotor interaction. Appl Acoust 2020;165(107308):107308.

[15] Pestana M, Sanjosé M, Moreau S, Roger M, Gruber M. Investigation on the noise of an axial low Mach-number fan stage with a heterogeneous stator. In: International conference on fan noise, aerodynamics, applications and systems; 2018.

[16] Pestana M. Effets de stators hétérogénes sur le bruit d'interaction rotor-stator: étude analytique, expérimentale et numérique. Ph.D. thesis. Université de Lyon; 2020.

[17] Tyler JM, Sofrin TG. Axial flow compressor noise studies. In: SAE technical paper series, SAE international, 400 commonwealth drive; 1962.

[18] Zhu T, Lallier-Daniels D, Sanjosé M, Moreau S, Carolus T. Rotating coherent flow structures as a source for narrowband tip clearance noise from axial fans. J Sound Vib 2018;417:198–215.

[19] Marsan A, Lallier-Daniels D, Sanjosé M, Moreau S, Mann A. Tip leakage flow and its implication on the acoustic signature of a low-speed fan; 2018.

[20] Ghodake D, Sanjosé M, Moreau S, Henner M. Effect of sweep on axial fan noise sources using the lattice Boltzmann method. Int J Turbomach Propuls Power 2022;7(4):34.

[21] Feng J, Bian T, Han Q, Wang B. A numerical investigation on the influence of the circular ring on the aerodynamic noise generated by a cooling fan. FDMP Fluid Dyn Mater Process 2023;19(1):1–14.

[22] Piellard M, Coutty BB, Goff VL, Vidal V, Perot F. Direct aeroacoustics simulation of automotive engine cooling fan system: effect of upstream geometry on broadband noise. In: 20th AIAA/CEAS aeroacoustics conference. American Institute of Aeronautics and Astronautics; 2014.

[23] Kohout D, Hyhlik T. Influence of the shroud leading edge shape on the axial-fan noise. In: Proceedings of the 6th world congress on mechanical, chemical, and material engineering. Avestia Publishing; 2020.

[24] Benedek T, Vad J, Lendvai B. Combined acoustic and aerodynamic investigation of the effect of inlet geometry on tip leakage flow noise of free-inlet free-exhaust low-speed axial flow fans. Appl Acoust 2022;187:108488.

[25] Zhu T, Carolus TH. Axial fan tip clearance noise: experiments, lattice-Boltzmann simulation, and mitigation measures. Int J Aeroacoust 2018;17(1–2):159–83.

[26] Lallier-Daniels D, Piellard M, Coutty B, Moreau S. Aeroacoustic study of an axial engine cooling module using lattice-Boltzmann simulations and the ffowcs Williams and Hawkings' analogy. Eur J Mech B, Fluids 2017;61:244–54.

[27] Longhouse RE. Noise mechanism separation and design considerations for low tip-speed, axial-flow fans. J Sound Vib 1976;48(4):461–74.

[28] Roger M, Moreau S. Aeroacoustic installation effects in cooling fan systems part 1: scattering by surrounding surfaces. In: The 12th international symposium on transport phenomena and dynamics of rotating machinery; 2008.

[29] Moreau S, Marck O, M R. Aeroacoustic installation effects in cooling fan systems part 2: near field and ground effect. In: The 12th international symposium on transport phenomena and dynamics of rotating machinery; 2008.

[30] Lu Y-Y. Experimental study of installation effects on cooling fan noise; 2021.

[31] Foss J, Neal D, Henner M, Moreau S. Evaluating CFD models of axial fans by comparisons with phase-averaged experimental data. In: SAE technical paper series, SAE international, 400 commonwealth drive, Warrendale, PA, United States; 2001.

[32] Sturm M, Sanjose M, Moreau S, Carolus T. Aeroacoustic simulation of an axial fan including the full test rig by using the lattice Boltzmann method. In: FAN 2015: international conference on fan noise, technology and numerical methods. London: Institution of Mechanical Engineers; 2015.

[33] Bellelli F, Arina R, Avallone F. On the impact of operating conditions and testing environment on the noise sources in an industrial engine cooling fan. In: 30th AIAA/CEAS aeroacoustics conference (2024); 2024. p. 3011.

[34] He X, Luo L-S. Theory of the lattice Boltzmann method: from the Boltzmann equation to the lattice Boltzmann equation. Phys Rev E, Stat Phys Plasmas Fluids Relat Interdiscip Topics 1997;56(6):6811.

[35] Sanjose M, Lallier-Daniels D, Moreau S. Aeroacoustic analysis of a low-subsonic axial fan, vol. 1: aircraft engine; fans and blowers; marine of turbo expo: power for land, sea, and air; 2015.

[36] Perot F, Moreau S, Kim M-S, Henner M, Neal D. Direct aeroacoustics predictions of a low speed axial fan. In: 16th AIAA/CEAS aeroacoustics conference. American Institute of Aeronautics and Astronautics; 2010.

[37] Perot F, Kim M-S, Moreau S, Henner M. Axial fan noise aeroacoustics predictions and inflow effect on tonal noise using LBM. In: CFD Canada 2013 conference; 2013.

[38] Bhatnagar PL, Gross EP, Krook M. A model for collision processes in gases. I. Small amplitude processes in charged and neutral one-component systems. Phys Rev 1954;94(3):511–25.

[39] Chapman S, Cowling TG. Cambridge mathematical library: the mathematical theory of non-uniform gases: an account of the kinetic theory of viscosity, thermal conduction and diffusion in gases. Cambridge, England: Cambridge University Press; 1991.

[40] Qian YH, D'Humières D, Lallemand P. Lattice BGK models for Navier-Stokes equation. Europhys Lett 1992;17(6):479–84.

[41] Zhang R, Sun C, Li Y, Satti R, Shock R, Hoch J, et al. Lattice Boltzmann approach for local reference frames. Commun Comput Phys 2011;9(5):1193–205.

[42] Chen H, Kandasamy S, Orszag S, Shock R, Succi S, Yakhot V. Extended Boltzmann kinetic equation for turbulent flows. Science 2003;301(5633):633–6.

[43] Teixeira CM. Incorporating turbulence models into the Lattice-Boltzmann method. Int J Mod Phys C 1998;09(08):1159–75.

[44] Launder BE, Spalding DB. The numerical computation of turbulent flows. Comput Methods Appl Mech Eng 1974;3(2):269–89.

[45] Williams JEF, Hawkings DL. Sound generation by turbulence and surfaces in arbitrary motion. Philos Trans R Soc Lond 1969;264(1151):321–42.

[46] Casalino D. An advanced time approach for acoustic analogy predictions. J Sound Vib 2003;261(4):583–612.

[47] Farassat F, Succi GP. The prediction of helicopter rotor discrete frequency noise. AHS; 1982. p. 497–507.

[48] Casalino D, Grande E, Romani G, Ragni D, Avallone F. Definition of a benchmark for low Reynolds number propeller aeroacoustics. Aerosp Sci Technol 2021;113(106707):106707.

[49] Welch P. The use of fast Fourier transform for the estimation of power spectra: a method based on time averaging over short, modified periodograms. IEEE Trans Audio Electroacoust 1967;15(2):70–3.

[50] Avallone F, Ragni D, Casalino D. On the effect of the tip-clearance ratio on the aeroacoustics of a diffuser-augmented wind turbine. Renew Energy 2020;152:1317–27.

[51] Richardson LF. The approximate arithmetical solution by finite differences of physical problems involving differential equations, with an application to the stresses in a masonry dam. Philos Trans R Soc Lond 1911;210(459–470):307–57.

[52] Avallone F, van der Velden W, Ragni D, Casalino D. Noise reduction mechanisms of sawtooth and combed-sawtooth trailing-edge serrations. J Fluid Mech 2018;848:560–91.

[53] Roache PJ. Perspective: a method for uniform reporting of grid refinement studies; 1994.

[54] Lallier-Daniels D, Moreau S, Sanjose M. Aeroacoustics of a low-speed free tip fan with a complex clearance geometry. In: Volume 13: vibration, acoustics and wave propagation. American Society of Mechanical Engineers; 2014.

[55] Nardari C, Casalino D, Polidoro F, Coralic V, Lew P-T, Brodie J. Numerical and experimental investigation of flow confinement effects on uav rotor noise. In: Vol. 25th AIAA/CEAS aeroacoustics conference; 2019.

[56] Zhu T, Carolus T. Experimental and numerical investigation of tip clearance noise of an axial fan using a lattice Boltzmann method, FAN; 2015.

[57] Kim M-S, Pérot F, Mann A, Choi E-S, Cho M-H, Kim J-H. Automotive engine cooling fan noise prediction using a lattice Boltzmann based method. FISITA World Congress; 2016.